Measuring the functional complexity of nanoscale connectomes: polarity matters

Qingyang Wang*[1], Nadine Randel[2,4,5], Yijie Yin[3,4,5], Cameron Shand[6], Amy Strange[6], Michael Winding[6], Albert Cardona[2,4,5], Marta Zlatic[3,4,5], Joshua T. Vogelstein[7,1], and Carey E. Priebe[8]

[1]Department of Neuroscience, Johns Hopkins University
[2]Department of Physiology, Development, and Neuroscience, University of Cambridge
[3]Department of Zoology, University of Cambridge
[4]MRC Laboratory of Molecular Biology, Neurobiology Division
[5]Janelia Research Campus, Howard Hughes Medical Institute
[6]The Francis Crick Institute, London, United Kingdom
[7]Department of Biomedical Engineering, Johns Hopkins University
[8]Department of Applied Mathematics and Statistics, Johns Hopkins University, United States

The emerging electron microscopy connectome datasets provides connectivity maps of the brains at single cell resolution, enabling us to estimate various network statistics, such as connectedness. We desire the ability to assess how the functional complexity of these networks depends on these network statistics. To this end, we developed an analysis pipeline and a statistic, XORness, which quantifies the functional complexity of these networks with varying network statistics. We illustrate that actual connectomes have high XORness, as do generated connectomes with the same network statistics, suggesting a normative role for functional complexity in guiding the evolution of connectomes, and providing clues to guide the development of artificial neural networks.

1 Introduction

How do brains support complex behaviors? Despite the significant advancements in neuroscience, it remains challenging to identify the fundamental wiring rules or structural properties that are necessary for complex functionalities.

Part of the difficulty lies in expanding the repertoire of structural properties to be studied. Although graph and network theory offer many valuable insights into which network properties might be critical [1, 2], many of these properties are hard to estimate without large-scale, synapse-level connectivity data. Even basic graph metrics, such as in-degree (the number of pre-synaptic neurons), cannot be accurately determined without a complete synapse-level connectivity map. The recent emergence of nanoscale electron microscopy (EM) connectomes solve this problem, enabling analysis at an unprecedented level [3–11].

Another challenge arises from the generality of the concept of functional complexity, rendering it difficult to define or quantify without relying on specific behaviors or tasks. Statistical theories, such as Vapnik–Chervonenkis dimension and Rademacher Complexity [12] offer analogous means of defining functional complexity; yet, they depend on exhaustive metrics that are difficult to translate into experimentally testable measurements. To address this, we propose a functional complexity measurement that is task-agnostic, learning-independent, and experimentally testable.

The brain structure property we focus on is the Excitatory-Inhibitory (E-I) neuron ratio. Although basic, the E-I ratio is highly conserved across species. Yet, its functional significance remain poorly understood. Across a wide range of species—from *Drosophila* [4, 13], rodents [14–20], cats [21–23], to non-human primates [24], and humans [25]—excitatory neurons are the majority of neurons ($\sim$70-90%, Figure 6A). This Excitatory-Inhibitory (E-I) ratio is also conserved across different functional regions of the neocortex [14, 21, 24, 25]. What is the necessity of having so many excitatory neurons? Our results offer a clue.

By sampling many thousands of recurrent neural networks (RNNs) constrained by the larval and adult *Drosophila* EM connectome [3] and quantifying their functional complexity, we demonstrate that the optimal E-I ratio that maximizes functional complexity favors a high proportion of excitatory neurons: the top 1% networks have an

*qwang88@jhu.edu

average of $>$70% excitatory neurons. Furthermore, we demonstrate that the differential connectedness between excitatory and inhibitory neurons—inhibitory neurons tend to have more connections—also interplays with E-I ratio to optimize the overall functional complexity of networks. The E-I ratio and connectedness distribution of the top functional complexity simulations closely mirrors that of real brains. In the end, we close the loop by applying the insights extracted from EM connectome to solve a challenging scenario in artificial intelligence.

2 Results

2.1 Measuring functional complexity based on nonlinearity

We give the full detail of the functional complexity measurement in Section 4; here, we focus on building the intuition and reasoning behind the measurement. Consider an illustrative example where an animal has to classify toxic versus edible leaves (a binary classification problem). In *world alpha*, toxic leaves are always red regardless of shape (Figure 1B left two illustrations). In *world beta*, toxic leaves (class A solid) could be either green straight or red curved; edible leaves (class B dashed) could be either green curved or red straight. *World beta* requires solving more complicated function, because it cannot be solved with a linear function.

World beta is actually a description of XOR, a binary classification problem that involves two dimensional input and a binary output. In fact, any binary classification task that is dependent on both features is an XOR task [26]. Multiple animal behavior studies have shown that XOR is more challenging for humans and monkeys to learn compared to linearly solvable tasks [26–29]. Even in machine learning research, XOR has played a pivotal role in revealing the functional complexity of networks: the first AI winter started when Minsky and Papert pointed out perceptrons cannot solve XOR [30]. XOR has also revealed the functional significance of specific network structure: in prior work we proved that networks with non-decreasing activation functions (e.g. ReLU) and without any negative weights (equivalent to inhibitory connections) cannot solve XOR and thus are not universal approximators[1] [34].

Given a network with n neurons, out of which $|\mathcal{I}|$ are input neurons and $|\mathcal{O}|$ are output neurons, we measure its functional complexity by considering how many subnetworks can readily solve XOR, termed XORable subnetworks. The more XORable subnetworks, the more nonlinear input associations the network is able to form and the more complex decision boundaries the network can represent. A subnetwork is defined by the input-output combination $\{I_1, I_2, O\}$, which implicitly considers all the possible paths connecting the two input neurons to the output neuron within certain number of time steps. The procedure for deciding whether a subnetwork is XORable is illustrated in Figure 1D. Briefly, four independent simulations are run where the two input neurons are combinatorially activated at time 0 (left panel), corresponding to the four quadrants of the 2D input space (Figure 1C). The subnetwork $\{I_1, I_2, O\}$ is XORable when the output activity of the four simulations follow a particular order: the two simulations where both input neurons are simultaneously activated or not activated (solid borders in Figure 1C-D) should elicit output response that is linearly separable from the simulations where only one of the input neurons was activated. We iterate through all concerned subnetworks with the above procedure to obtain the functional complexity measurement.

We did not involve any parameter optimization in the functional complexity measurement: the connectome already encapsulates knowledge from evolution and life experiences, and our goal is to quantify the functional complexity on connectivity structures that is naturally present.

2.2 EM-constrained RNNs of varied E-I configurations show varied functional complexity

The recurrent neural network (RNN) (details in Section 4) is constrained by the larva *Drosophila* EM connectome [3]. There are in total 2952 neurons that form a connected graph (one single connected component), 400 of which are output neurons (RGNs and descending neurons) and 480 are input neurons. We will focus on olfactory (46) and gustatory (131) neurons as input throughout this paper. The neurons' firing rates $\mathbf{r}$ at time t are modeled as

$$\mathbf{r}(t) = ReLU(\mathbf{W}^T\mathbf{r}(t-1) + \mathbf{E}^{(t)}),\ t \in \{1 \dots T\}. \tag{1}$$

[1] Universal approximation theory is the foundational theoretical guarantee that helped to catapult deep learning out of the first AI winter [31–33].

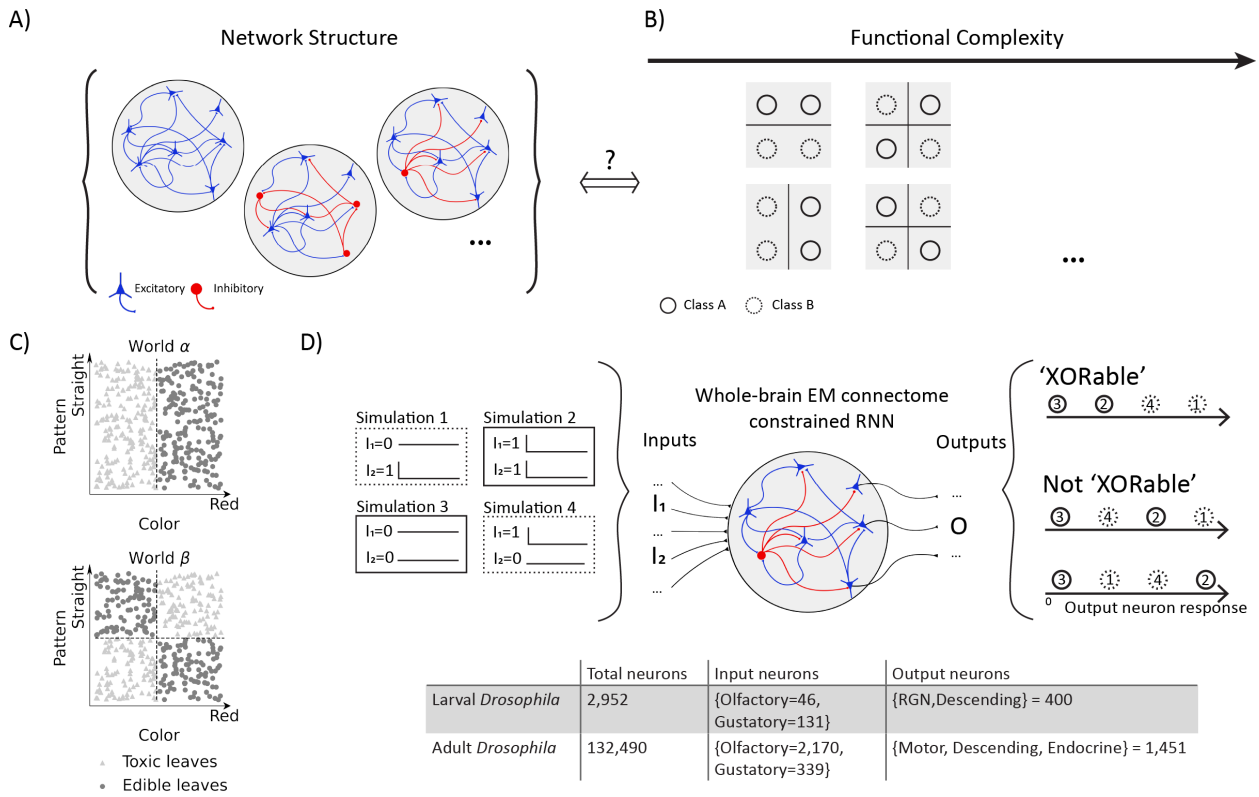

	Total neurons	Input neurons	Output neurons
Larval *Drosophila*	2,952	{Olfactory=46, Gustatory=131}	{RGN,Descending} = 400
Adult *Drosophila*	132,490	{Olfactory=2,170, Gustatory=339}	{Motor, Descending, Endocrine} = 1,451

Figure 1: **Proposed methodology to measure functional complexity of a given network.** A) Illustration on relating network structure, specifically E-I composition, to the network's functional complexity. B) XOR is a binary classification that takes two inputs, with the desired output being the two scenarios where only one of the two inputs is activated are classified into the same class (second and forth quadrant, dashed circles). Whether a subnetwork is 'XORable' serves as the building block of the functional complexity measurement and it can be tested by four independent input stimulation pairs. C) Given an EM-constrained larval *Drosophila* whole-brain RNN (2952 neurons in total, E-I composition sampled as detailed in Section 4), we iterate through the subnetworks $\{I_1, I_2, O\}$ where each subnetwork is defined by $\{I_1, I_2\}$ as two input neurons and O as the output. Exhaustively, we measure through all olfactory and gustatory neurons as inputs and all 400 output neurons (RGN and descending neurons). Whether a subnetwork $\{I_1, I_2, O\}$ is XORable is tested by the following procedure: four independent simulations are run (illustrated on the left and in panel C). The four simulation inputs correspond to $\{(0,1),(1,1),(0,0),(1,0)\}$ respectively, where 1 means the input neuron is activated. XORable corresponds to the situation where simulations 1 and 4 elicit output response that is linearly separable from simulations 2 and 3. In another word, the relative order of 1 and 4 should be larger than 2 and 3. This is illustrated on the right along with counter-examples.

$\mathbf{E}$ is the external stimuli in Figure 1D. The connectivity from pre-synaptic neurons to post-synaptic neurons, $\mathbf{W}$, is the element-wise product of two components: 1) the strength of connections $\mathbf{M}$, which is given by the synaptic count from the EM dataset (axon-dendrite synapses in main text; all-all connection results in the supplementary); and 2) the excitatory/inhibitory identity $\boldsymbol{\alpha}$ of each neuron which is randomly sampled.

The 2D XOR patterns were presented to the model by either stimulating two olfactory neurons (Figure 2 second column), two gustatory neurons (third column), or one olfactory paired with one gustatory neuron (rightmost column). We first varied E-I ratio by uniform Bernoulli sampling (horizontal lines in left column), i.e. all neurons have the same probability p of being excitatory. As a sanity check of our method, consider the extreme case where all neurons are excitatory: previous theoretical results predicted no XORable subnetwork exists in this scenario [34]. This is exactly what we observed, when E/(E+I)=1 we observed zero functional complexity across all panels. The optimal E-I ratio that maximized functional complexity fell between $\sim$50-60% excitatory neurons. In real larval brains, the ratio is closer to 67% [13].

This discrepancy prompted us to think maybe considering E-I ratio alone was insufficient, therefore we designed a

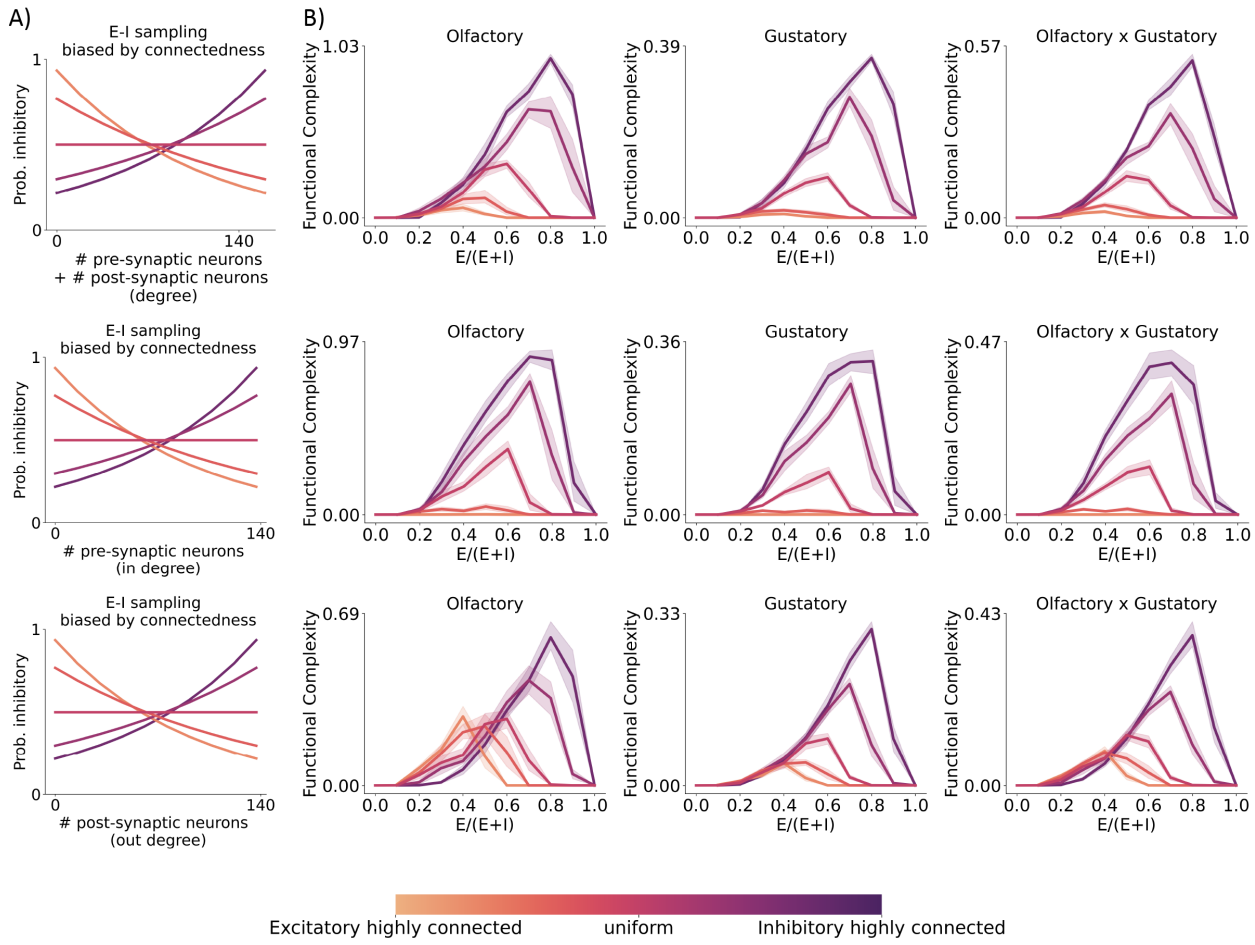

Figure 2: **The optimal E-I ratio that maximizes functional complexity is dependent on the connection degree of inhibitory neurons.** A) E-I probability as a function of its connectedness, quantified as either in degree (number of pre-synaptic neurons), out degree (number of post-synaptic neurons), or degree (in+out). For each neuron, the probability for it being sampled as inhibitory depends on its connectedness. All colored curves result in a target E-I ratio of 0.5 but with different extent of biasing the inhibitory population to be highly connected (noted by the colors given in the bottom colorbar). Darker colors = inhibitory neurons are more highly connected; Lighter colors = excitatory neurons are more highly connected. B) The resultant functional complexity with E-I identities sampled at various E-I ratio levels (x-axis) and various connectedness bias levels (colors). Shaded area mark the 95% confidence interval (n=10). When the E-I identity is uniformly sampled across all neurons (horizontal line in A and the curves of middle color in B), the optimal E-I ratio that maximizes functional complexity is $\sim$60% excitatory, across sensory modalities. However, the maximum level of functional complexity reached by uniform sampling is sub-optimal; more optimal E-I compositions require the sampling procedure to bias the inhibitory neurons to be highly connected (darker colors). In contrast, when the E-I sampling procedure shifts the excitatory neurons to be highly connected (lighter colors), it generally results in lower functional complexity.

procedure to sample the E-I identities as a degree dependent function (Figure 2A): for each neuron, the probability of it being sampled as inhibitory is dependent on its connectedness (details in Section 4). Ubiquitous evidence from the mouse cortex showed that inhibitory neurons are broadly tuned integrating diverse input [35–37] and sending out inhibition broadly [38, 39]. Therefore we quantified the connectedness of neurons in three ways: in degree (# pre-synaptic neurons) quantifying integration diversity, out degree (# post-synaptic neurons) quantifying output diversity, degree (# pre-synaptic neurons + # post-synaptic neurons) combining both. With the connectedness-dependent sampling procedure, we systematically varied the network structure from having highly connected excitatory neurons (lighter colors) to having highly connected inhibitory neurons (darker colors). Intriguingly, as the network structure shifted from highly connected excitatory neurons to highly connected inhibitory neurons

(light → dark), the optimal E-I ratio peak gradually shifted from 30-40% to 80% (Figure 2B). Furthermore, the overall optimality is achieved when the inhibitory neurons are highly connected and at 80% E-I ratio. These two observations hold across input sensory modalities (columns), and for both integration connectedness and output connectedness (rows).

These results suggest to achieve high functional complexity, it is desirable to have a good fraction of excitatory neurons, with inhibitory neurons receive broad input and output broadly. Although these results are based on axon-dendrite synaptic counts, they still hold when the connection magnitudes are given by all synapse types, i.e. axo-dendritic, axo-axonic, dendro-dendritic, and dendro-axonic (Figure A.3).

2.3 The RNNs with highest functional complexity match the E-I ratio and degree distribution of real brains

Does our observation from the previous sections generalize? That is, is it generally true that networks with over-abundance of excitatory neurons and highly-connected inhibitory neurons enjoy higher functional complexity? Next we quantified the functional complexity of an extensive set of EM connectome-constrained networks of various E-I configurations sampled by various forms of connectedness-dependent sampling procedures, including ones where the trend is not monotonic, i.e. neurons of mid-level connectedness having high probability of being inhibitory/excitatory (details in Section 4). In total, we performed 818 different types of sampling procedures according to different connectedness-dependent E-I probability functions, each type with 10 different samples (Figure 3). Notably, networks of higher functional complexity (lighter color) not only have an over-abundance of excitatory neuron population (x-axis > 0.5, right to vertical gray line), they also have more highly connected inhibitory population compared to the excitatory population (y-axis > 0, above horizontal gray line). The degree difference between inhibitory and excitatory population is evident when considering input integration (middle column, more in Supplementary Figure A.10,A.12), output breadth (right column, more in Supplementary Figure A.14,A.16), or combined (left column, more in Supplementary Figure A.8). They also hold across input from different sensory modalities (Supplementary Figure A.6, A.7, A.9, A.11, A.13, A.15).

Do the network structural predictions based on functional complexity match to real brain observations? Yes. The real larva measurements (green stars in Figure 3A,B) fall within the region of networks with high functional complexity. In terms of the E-I ratio prediction, the top 1% networks of highest functional complexity have on average 72% of excitatory neurons. The distribution of the E-I ratio of the highest sampled networks closely aligns with the real brain E-I ratios obtained by scRNA-seq [13](green stars x-value in Figure 3A and first column in C). This is true regardless of the exact criterion for selecting the *top* simulations (Figure 3C): the result holds when comparing brain data to top 1% simulations (p-val 0.98, Dunnett's [40]); it also holds when comparing to the top 13 probability function group averaged E-I ratios (p-val 0.40, Dunnett's). When comparing the real brain E-I ratio distribution with all simulations, the means are statistically significantly different (p-val: 0.03, Dunnett's). The top functional complexity simulations' match to real brain E-I ratios not only hold for networks sampled by degree (in+out), but also hold for networks sampled by in degree (Figure A.10C) as well as out degree (Figure A.14C); the match also holds when the connection weight is given by synapse counts of all synapse types (Figure A.8C, A.12C, A.16C).

To check if the inhibitory neurons tend to be more highly connected in real brains, we need to obtain the E-I identities of the whole-brain EM connectome. In another study (unpublished data), we identified the neurotransmitters for a subset of neurons (170 acetylcholine as excitatory neurons, 156 GABAergic and 26 glutamatergic as inhibitory neurons), marked by the green stars in Figure 3A . Since the selection of the subset is not representative of the whole-brain E-I ratio, we marked the x-axis by scRNA-seq data. Although the subset of neurons with known E-I identities are not selected randomly, their connection properties still exhibit trend matching predicted networks of higher functional complexity (upper right quadrant). In a separate study, we used these known neurotransmitter identities to predict for the rest of the neurons via machine learning method [41], identifying 1917 acetylcholine as excitatory neurons, 160 GABAergic and 857 glutamatergic as inhibitory neurons (unpublished data, the model's accuracy was 98% for acetylcholine, 59% for GABAergic, and 78% for glutamate expressing neurons). The predicted whole-brain E-I identities are marked by the green stars in Figure 3B, with the color inside the star indicating the measured functional complexity based on the predicted whole-brain E-I identities. Again, the whole-brain observations match to the predicted networks of higher functional complexity (Figure 3D). To account for potential E-I prediction errors, we shuffled the E-I identities of neurons with low prediction confidence (second

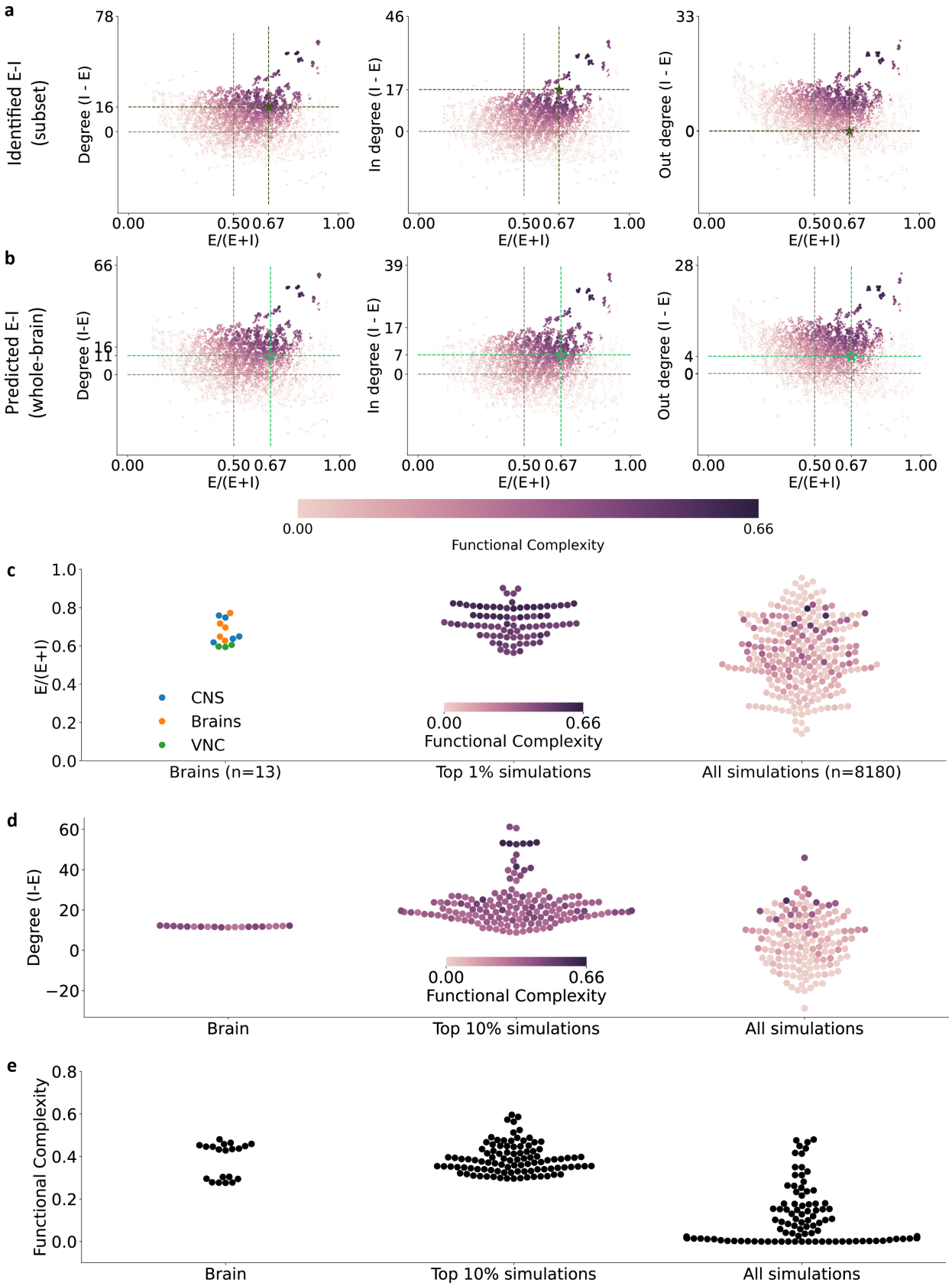
a
Identified E-I (subset)
Degree (I - E)
In degree (I - E)
Out degree (I - E)
E/(E+I)
b
Predicted E-I (whole-brain)
Degree (I-E)
Functional Complexity
c
E/(E+I)
CNS
Brains
VNC
Brains (n=13)
Top 1% simulations
All simulations (n=8180)
d
Degree (I-E)
Brain
Top 10% simulations
All simulations
e
Functional Complexity

Caption on next page →

Figure 3: **The top simulations of highest functional complexity match the E-I ratio distribution observed in real larval *Drosophila* brains.** A-B) 8180 different E-I compositions are drawn from 818 different connectedness-dependent E-I probability functions (10 samples each). Networks of higher functional complexity (lighter color) lie on the upper right quadrant where the average connectedness of inhibitory neurons are higher than excitatory neurons (y-axis > 0, above horizontal gray line) and there is an over-abundance of excitatory neurons (x-axis > 0.5, right to vertical gray line). Left to right: differential connectedness of inhibitory and excitatory neurons are measured by degree (in+out), out degree, and in degree respectively. The green stars mark real brain measurements: top (A) x-axis given by scRNA-seq measurements [13] and y-axis given by neurons in the EM connectome with known E-I identities (unpublished data); bottom (B) given by all neurons in the EM connectome with predicted E-I identities (unpublished data) C) Left: E-I ratios of 13 larval *Drosophila* obtained via scRNA-seq, colored by the source region; Middle left: the E-I ratios of top 13 simulations obtained via averaging across the 10 samples of each connectedness-dependent E-I probability function group (details see Supplementary Figure A.17); Middle right: the E-I ratios of top 1% simulations; Right: E-I ratios of all simulations. The mean E-I ratio of the top 13 group-averages and top 1% simulations are *not* statistical significantly different from the 13 brain E-I ratios (two-sided two-sample t-test, p-val: 0.98, 0.51 respectively). Multiple comparisons corrected by Dunnett's. D) Same as C except for the differential connectedness of inhibitory and excitatory neurons, i.e. Degree (I-E), the brain data is based on EM connectome E-I predictions. E) Same as C except for the functional complexity.

column in Figure 3D) and did not find it to complicate the conclusion.

Given the whole-brain E-I predictions, we also measured its functional complexity as well as for the low-prediction-confidence shuffled networks (Figure 3E) - they all match to the functional complexity range of the top 10% simulations. These suggest real larval *Drosophila* brain indeed enjoy high functional complexity.

Of note, the functional complexity measurement that we propose is the key in revealing these patterns — a conventional norm-based method such as the participation ratio and spectral norm fail to do so (Supplementary Figure A.5).

Collectively, our extensive simulation results point out two important network structure properties in supporting high functional complexity: 1) over-abundance of excitatory neurons; and 2) highly connected inhibitory neurons. Furthermore, such structural properties selected by functional complexity match to real brain observations.

2.4 Results generalize across developmental stages to adult *Drosophila*

To test if our results generalize across developmental stages, we performed the same functional complexity analysis in the adult *Drosophila* whole-brain EM connectome (FlyWire [4]). The FlyWire dataset has 132,490 neurons in total, with 2,170 olfactory neurons, 339 gustatory neurons, and 1,451 output neurons (motor, descending, and endocrine). The adult whole-brain network is orders of magnitudes larger than the larval EM connectome, therefore sub-sampling was adopted to accommodate for the computation requirements (details in Section 4).

We sampled 703 different E-I compositions from 235 different connectedness-dependent E-I probability functions (Figure 4A-B). Although the sampling procedure is carried out in a smaller scale compared to what we did for the larvae, the resultant network structures still span the full feature space under investigation, i.e. E-I ratio and differential connectedness between inhibitory and excitatory populations. The results in adult *Drosophila* show striking similarity to what was observed in the larvae: First, across different input sensory modalities (Figure 4A), higher functional complexity (lighter color) for RNNs constrained by the adult *Drosophila* connectome is associated with both over-abundance of excitatory neuron population (x-axis > 0.5) as well as highly connected inhibitory population compared to the excitatory population (y-axis > 0). Second, as in the larvae, we observe a preference for more highly connected inhibitory neurons (Figure 4B) when we consider the input integration (middle), output breadth (right) and combined (left).

Furthermore, such predictions based on highest functional complexity also match to real brain observations (green stars). First, the top 10% simulations with highest functional complexity have on average 79% excitatory neurons which is strikingly similar to the 74% average observed from real brains across two genotypes via scRNA-seq [42] (Figure 4C). To see if in the brain the inhibitory neurons in general tend to be more highly connected than excitatory neurons, we again calculated the population average difference (Figure 4D) and took care of the missing E-I predictions by random assignments (left column): indeed, on average, the inhibitory neurons connect with 15 more pre-synaptic and post-synaptic neurons than excitatory neurons. Furthermore, based on the E-I predictions on the

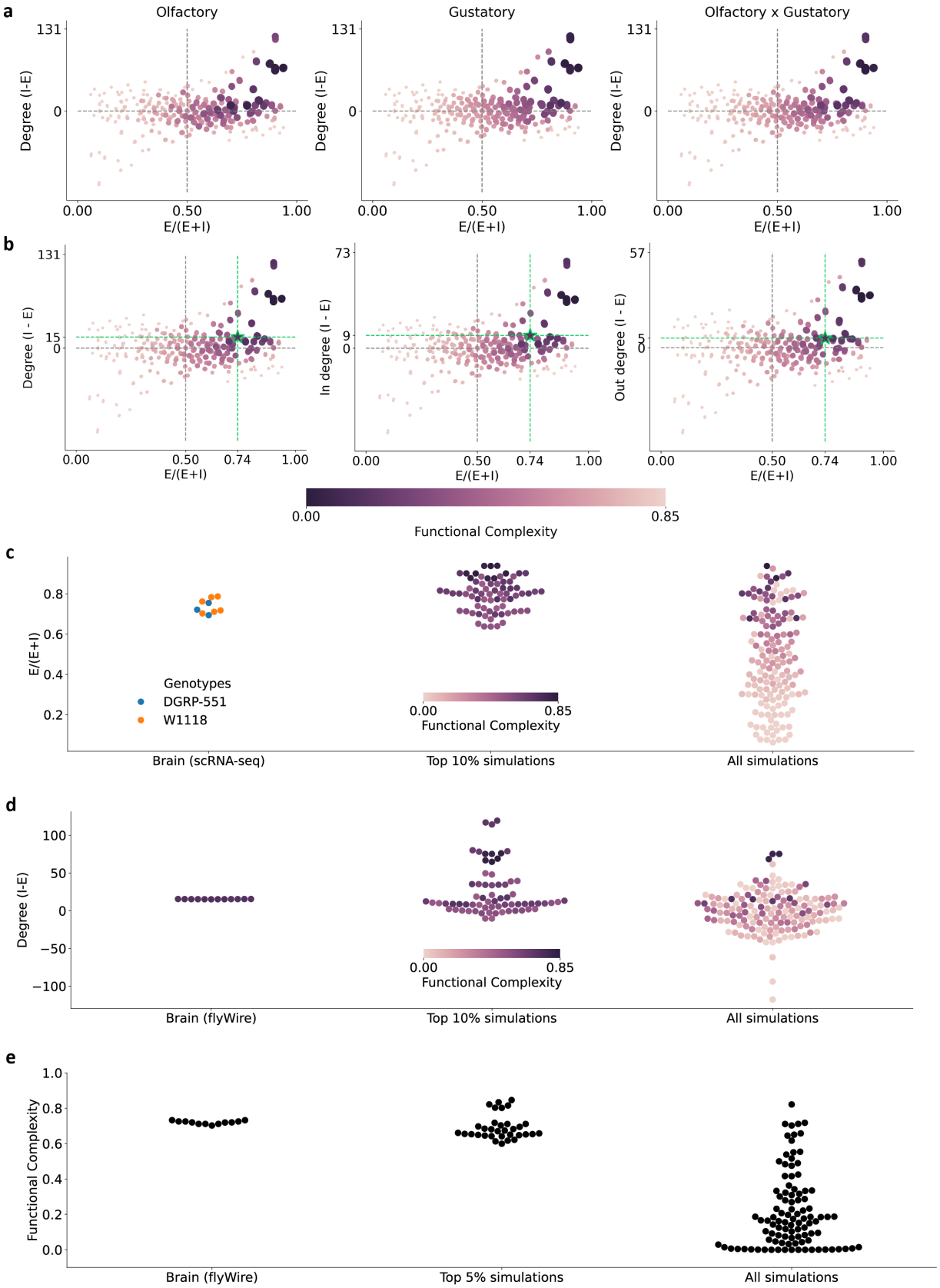
a
Olfactory
Gustatory
Olfactory x Gustatory
Degree (I-E)
E/(E+I)
b
Degree (I - E)
In degree (I - E)
Out degree (I - E)
Functional Complexity
c
E/(E+I)
Genotypes
DGRP-551
W1118
Brain (scRNA-seq)
Top 10% simulations
All simulations
d
Degree (I-E)
Brain (flyWire)
Top 10% simulations
All simulations
e
Functional Complexity
Brain (flyWire)
Top 5% simulations
All simulations

Caption on next page →

Figure 4: **The results generalize across developmental stages to adult *Drosophila*.** A-B) 703 different E-I compositions are drawn from 235 different connectedness-dependent E-I probability functions (3 samples each). As observed for the larvae, networks of higher functional complexity (lighter color) lie on the upper right quadrant where the average connectedness of inhibitory neurons are higher than excitatory neurons (y-axis > 0, above horizontal gray line) and there is an over-abundance of excitatory neurons (x-axis > 0.5, right to vertical gray line). A) Left to right: the observations hold across sensory modalities. B) Left to right: differential connectedness of inhibitory and excitatory neurons are measured by degree (in+out), out degree, and in degree respectively. The green stars mark real brain measurements given by neurons in the EM connectome with predicted E-I identities. C) Left: E-I ratios of 9 adult *Drosophila* (age 6d and 9d) obtained via scRNA-seq, colored by the genotypes (data from [42]); Middle left: E-I ratio based on FlyWire neurotransmitter predictions (each dot is a low-prediction-score shuffle); Middle: the E-I ratios of top 10% simulations; Right: E-I ratios of all simulations. D) Same as C except for the differential connectedness of inhibitory and excitatory neurons, i.e. Degree (I-E), the brain data is based on EM connectome E-I predictions. E) Same as C except for the functional complexity.

EM connectomes, the measured functional complexity score of real brains mounts to 0.71 on average, which is strikingly similar to the top 5% simulated networks which mounts to 0.72 on average.

Collectively, our functional complexity analysis on adult *Drosophila* whole-brain EM connectome provide a normative explanation to why across developmental stages, *Drosophila* tend to have over-abundance of excitatory neurons and highly-connected inhibitory neurons.

2.5 E-I structures identified from the connectome functional complexity analysis solves a challenging scenario in AI.

Our functional complexity analysis on larval and adult *Drosophila* EM connectomes suggest that over-abundance of excitatory neurons and highly-connected inhibitory neurons offer an advantage in representing complex functions. Could we leverage this insight to build AI that learn complex tasks better? We next tested these ideas in sparse networks. We focused on the setting where networks are highly sparse because 1) it has been a challenging setting for AI [43]; 2) adequate sign configurations (E-I configurations) *are* crucial in training sparse networks [44, 45]; and 3) biological networks are sparse, both the larval and adult *Drosophila* whole-brain connectomes are 99% sparse. We trained convolutional neural networks (CNNs) at 99% sparsity on Fashion-MNIST, a pattern recognition benchmark (Supplementary Figure A.19). The E-I configurations and wiring were either unconstrained or biologically constrained. In the unconstrained classical pruning scenario, both signs and wiring can be dynamically updated throughout the training process, enjoyings full flexibility (orange); In the biologically constrained scenarios, we asked the signs to follow Dale's principle, i.e. all output edges of the same neuron follow the same sign, and tested 3 E-I configuration settings: 1) 80% excitatory neurons with 4 times more highly connected inhibitory neurons (red); 2) 50% excitatory neurons with equally connection-degree E/I populations (blue); 3) 20% excitatory neurons with 4 times more highly connected excitatory neurons (green). These three scenarios are designed to achieve equal number of positive and negative weight entries.

Unconstrained sparse networks indeed have trouble learning the task (Supplementary Figure A.19**a**, orange), especially when the networks are deep (convDepth = 4, orange solid dots show significant inferior performance across the board), and have limited width (left two columns). In these challenging scenarios, CNNs that are biologically constrained to follow Dale's principle do *not* suffer from inferior performance (Supplementary Figure A.19**a**, red, blue, green). Furthermore, over-abundance of excitatory with highly-connected inhibitory neurons demonstrate an advantage over other E-I configurations in the more challenging settings. These are evident from the fact that 80% excitatory group (red) consistently achieve higher validation accuracy at convergence (higher in Figure 5**a**) and takes less number of iterations to achieve 75% validation accuracy (lower in Figure 5**b**). The computational efficiency advantage is independent of the accuracy cut-off selection (Supplementary Figure **??**). These results demonstrate that the E-I structures identified from our functional complexity analysis on EM connectomes offer solutions to train sparse networks effectively and computational efficiently.

3 Discussion

Why do we have so many excitatory neurons? Our answer is: to solve more complex functions. To measure functional complexity of networks, we proposed a normative measurement based on the nonlinearity of subnetwork

Figure 5: **Bio-realistic E-I configurations offer solutions to sparse network training problems. a** Sparse CNNs constrained by Dale's rule (red, blue, green) reach higher validation accuracy at convergence then classical pruning procedure (orange), with 80% excitatory setting (red) demonstrating an advantage in difficult settings where the network is narrow and deep (depth=4, width=[16, 24]), i.e. among darkest dots red always dominate. **b** 80% excitatory demonstrates an advantage in computation efficiency as it not only have higher chance of reaching 75% validation accuracy (less dots at the top 'not reached' section) but also take comparative or less number of epochs.

functions. We leveraged the larva and adult *Drosophila* EM connectome [3] and revealed a key structure property - connectedness of neurons - that alters the functional complexity of the resultant networks. The top E-I configurations with the highest functional complexity nicely matched the E-I ratio and degree distributions observed in real larva and adult*Drosophila* brains. It is worth pointing out that the calculation of degree for all neurons is *not* possible without the availability of the EM connectome data. This emphasizes on the importance of having the entire connectivity map, so that the unexplored but crucial structure properties and their interplay could be explored. We further applied the E-I structures identified from our functional complexity analysis on EM connectomes to offer solutions to train sparse networks effectively and computational efficiently.

The optimal E-I ratio has been previously explored in terms of the capacity on storing binary memory patterns [46]. The predicted optimal E-I ratio is a function of the degree of tuning (coefficient of variation) of the excitatory and inhibitory activities. Consequently, validating it requires knowing both the input statistics and the connectivity pattern. [47] had trained RNNs with sparse connections (out degree following a bio-plausible distribution) to sequentially learn multiple binary classification tasks; consistent with the normative answers provided here, they also found the optimal performing RNNs to have 70% excitatory neurons [47]. These suggest the functional complexity measurement proposed here may have direct implications on networks' capabilities in multi-task learning.

We deliberately set all bias terms of the RNN, i.e. threshold of the neurons, to be zero. The main reason is we did not want the biases to obscure the effects of the connectivity patterns. It is known that any dynamics' trajectory can be approximated arbitrarily well by a wide-enough RNN with fixed weights and learnt/well-chosen biases [48]. This means if we choose to learn the bias terms or even just randomly set them, there is a good chance the subnetwork can produce XORable dynamics; but then such observed XORable pattern is not due to the connectivity pattern but because of the non-zero biases, resulting in high false positives when checking for XORable subnetworks. This logic is further backed by the fact that XOR can be solved by a network with only three hidden units and all zero biases [49]; although the 2952 neurons are not fully connected to each other in our case, there is still a high chance non-zero biases will greatly increase the number of XORable subnetworks and obscure the effects from

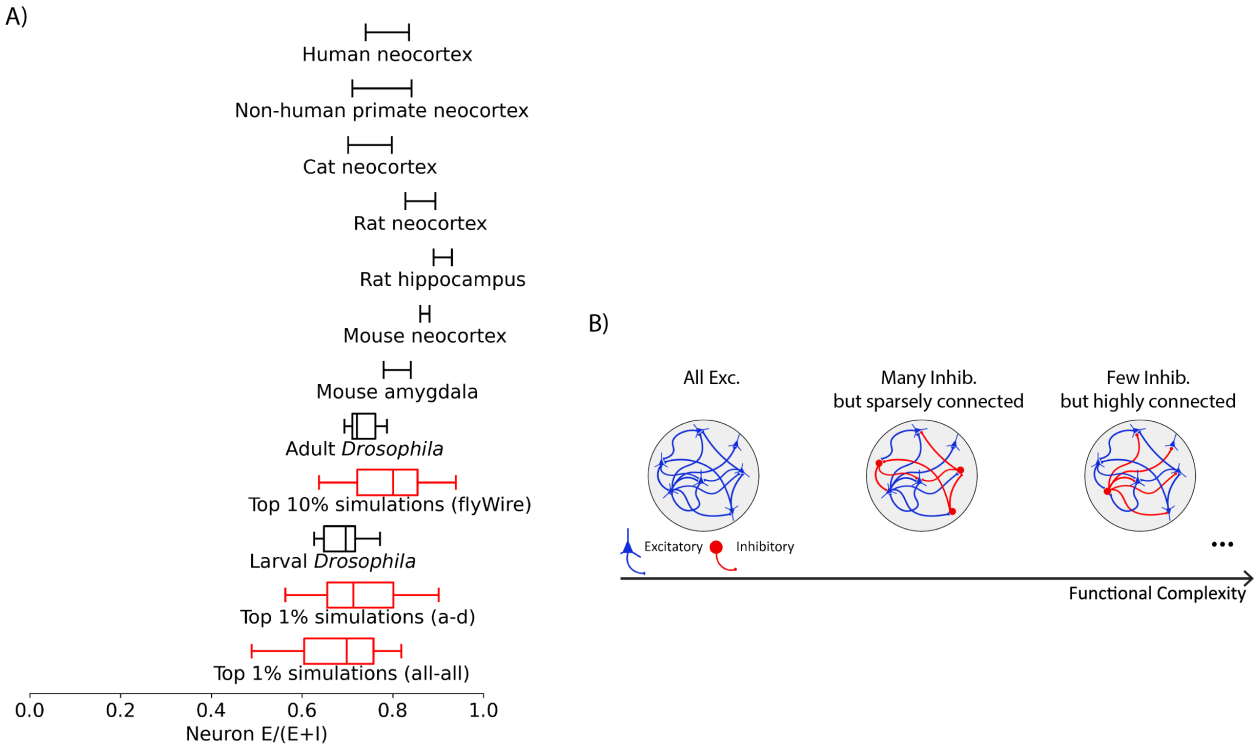

Figure 6: **Conceptual illustration on E-I composition and functional complexity.** A) The over-abundance of excitatory neurons is observed across a wide range of species (from Drosophila [4, 13, 42] to mouse neocortex and amygdala [14, 15] to rat neocortex [16–18] and hippocampus [19, 20], to cats [21–23] to non-human primates [24] to humans [25]). B) A conceptual illustration on the relationship between E-I composition and functional complexity.

the connectivity pattern. A dedicated separate study is required to carefully delineate the interplay between biases and connectivity pattern in terms of their effects on functional complexity.

The inspiring thread of work on manifold capacity touches upon the concept of representation complexity in classification settings [50–53]; however, the definition of complexity in manifold capacity fundamentally differ from the proposed functional complexity measurement, leading the two methods targeting completely different questions. Manifold capacity targets neuronal activity: essentially, a population of neurons has higher capacity when the desired output can be more readily linearly read-out for the pre-specified task output, leaving the discussion on the non-linearity part of the transformation implicit. In contrast, our functional complexity measurement directly measures the non-linearity of the network. Although the latest development incorporated non-linear classifications into the framework, it relies on context-dependent learning and the resultant capacity measurement is dependent on the definition of context [53]. In sum, manifold capacity focuses on neural representations and their linear readout; ours focuses on directly quantifying the non-linearity of networks.

In statistics and mathematics, some possible choices of quantifying the concept of functional complexity include Rademacher Complexity [54] and VC-dimension [55], which essentially measures the richness of a function class. However, neither can be directly applied because they quantify complexity of a function class, and we are interested in complexity of a particular function: the actual weights of a particular network. The proposed functional complexity measurement relates to VC-dimension in the sense that it considers the hardest problems (XOR like) out of the entire function set considered in VC-dimension (growth function to be precise) at 4 data points. In other words, our procedure takes the hardest slice of VC-dimension and makes an applicable measurement out of it.

The proposed functional complexity measurement is not just implementable *in silico*; it is also experimentally testable. With the high-throughput automated behavior technologies available for larval *Drosophila* [56, 57], one

could potentially optogenetically stimulate pairs of input neurons according to patterns illustrated in Figure 1D while recording from the output neurons, such as RGNs and/or descending neurons. It will be exciting to see if the fraction of XORable subnetworks in real larvae match the results obtained via EM-constrained simulations presented here.

An important future direction is to extend this analysis to other EM connectomes [7–11], exploring whether the E-I ratios of other species and in other contexts can also be explained by optimizing for high functional complexity. A comparative study across species would also be of interest. For example, it would be interesting to see if the proposed functional complexity measurement can explain for the expanded inhibitory subnetwork in humans compared to rodents [58]. Meanwhile, a macroscopic gradient of synaptic excitation and inhibition has been observed along the hierarchy of brain regions [59], making it interesting to see if there is also a gradient of functional complexity along the hierarchy of processing.

4 Methods

XORable subnetwork Consider a subnetwork defined by two input neurons I_1, I_2 and one output neuron O. It includes all possible paths connected between them. We are interested in checking if the binary classification problem XOR, depicted in Figure 1C, is readily solvable by the subnetwork $\{I_1, I_2, O\}$. To test this, four independent simulations are run (Figure 1D):

1. Simulation 1: only input neuron I_2 is activated at time zero;
2. Simulation 2: both input neurons are activated at time zero;
3. Simulation 3: both input neurons are *not* activated;
4. Simulation 4: only input neuron I_1 is activated at time zero.

The activity of the output neuron O is recorded for all time steps. At each times step, we compare the output activity of the four simulations (Figure 1D right panel) and their relative order determines whether the subnetwork is XORable. Specifically, the desired XORable order request simulations 2 & 3 (both input activated or not) to be linearly separable from simulations 1 & 4 (only one of the input activated). Since simulation 3 receives no input activation thus always having zero output, there are only two XORable ordering out of the six possible orderings in total (1 & 4 interchangeable in the illustration). As long as there is at least one time step that have XORable output order then we say the subnetwork is XORable.

Relative order of the four simulations' output neuron response	XORable?
3 < 1 < 2 < 4	n
3 < 1 < 4 < 2	n
3 < 2 < 1 < 4	y
3 < 2 < 4 < 1	y
3 < 4 < 1 < 2	n
3 < 4 < 2 < 1	n

Table 1: **All possible orders of output responses of the four simulations at each time step.** (related to Figure 1)

Functional Complexity The functional complexity measurement counts the fraction of input pair (I_1, I_2) that have a robust number ($\geqslant 20$) of XORable subnetworks associated with it, i.e. $\sum \mathbf{1}_{\{I_1, I_2, O\}\text{is XORable}} \geqslant 20$.

Whole-brain larval *Drosophila* EM connectome-constrained RNN The whole-brain neuronal activity of larval *Drosophila* is simulated with a biologically-constrained recurrent neural network (RNN). Concretely, the neurons' firing rates $\mathbf{r}$ at time t are given by

$$\mathbf{r}(t) = ReLU(\mathbf{W}^T\mathbf{r}(t-1) + \mathbf{E}^{(t)}),\ t \in \{1 \dots T\} \tag{2}$$

where $\mathbf{W}$ is the weight matrix describing the connections from pre-synaptic neurons to post-synaptic neurons, with the signs (E-I) sampled and the magnitudes given by the axon-dendrite synaptic count from the EM dataset [3] (all-all synaptic count results are given in supplementaries and are always consistent with the axon-dendrite results). $\mathbf{E}^{(t)}$ denotes the time-series external input delivered to the input neurons. All simulations were run for

$T = 20$ time steps, a duration long enough for the network dynamics to stabilize when single input neurons were initially activated.

Uniform sampling on E-I identities For a target E-I ratio p, where $p \in [0, 1]$, the E-I identity of each neuron is independently sampled from a Bernoulli distribution of probability p, which gives the signs of the columns of the weight matrix $\mathbf{W}$.

Connectedness-dependent sampling on E-I identities For each neuron with a connectedness of d (either degree, in degree, or out degree), its E-I identity is sampled from a Bernoulli distribution of probability p_d. The connectedness-dependent probability p_d is set as following: all neurons are grouped into deciles ($q \in [10]$) based on their connectedness, and each decile is assigned a probability p_d, forming a probability vector of length 10. In section 2.2, the probability vector is set following exponential function, i.e. $p_d \propto \beta^q$, and the base β controls the rate of biasness (Figure 2A). A linear relationship was also explored(Figure A.4), where $p_d \propto \beta \times q$ with β controlling the rate of biasness. In section 2.3, more connectedness-dependent probability vectors are explored by sampling non-monotone relationships. The most exhaustive way would be search in the $[0, 1]^10$ space for all possible probability vectors, which is computationally prohibitive. Instead, we explored a subset of all length-10 probability vectors featuring various peak positions. Specifically, we generated single-peak probability vectors where the first, fifth and last elements take values from [0, 0.25, 0.5, 0.75, 1], [0, 0.1, 0.2, 0.3, 0.4, 0.5, 0.6, 0.7, 0.8, 0.9, 1], and [0, 0.25, 0.5, 0.75, 1] respectively. The fifth element is constrained to be the extrema, resulting in 184 distinct probability vectors. In addition, three other groups of single-peak vectors were created by shifting the peak two deciles higher, two deciles lower, or five deciles.

Real brain E-I ratios. The scRNA-seq data were obtained from [13] where 13 individuals were collected for their brains, ventral nerve cord (VNC) or the entire central nervous system (CNS = brain + VNC). Cholinergic cells and Kenyon cells were considered as excitatory. For CNS and VNC samples, only GABAergic cells were considered as inhibitory. For brain samples, glutamatergic cells were additionally considered to be inhibitory.

E-I prediction low prediction confidence shuffle. In unpublished work, the whole-brain EM connectome neurotransmitter identities are predicted from known subset, leveraging machine learning method [41]. The neurotransmitter prediction of each neuron is associated with a set of confidence scores of the 3 neurotransmitter choices: Acetylcholine, GABAergic, Glutamatergic. Neurons with the maximum confidence score < 0.4 are shuffled for their E-I identities. The shuffling was done 20 times independently.

Adult *Drosophila* whole-brain EM connectome analysis. All analysis procedures follow larval *Drosophila*, with the following adaptations. The synaptic counts and neurotransmitter predictions are accessed from FlyWire v783 [4], which determines the connection strengths and signs respectively. Only the largest connected component in the constructed whole-brain graph is included in the analysis (132,490 neurons in total with 118,534 neurons with neurotransmitter predictions). All connection strengths are normalized to the percentage of total input onto a given target neuron.

Since the adult *Drosophila* network is two magnitudes larger than the larvae, we had to sub-sample in our functional complexity analysis. Instead of exhaustively iterate through all input combinations as for the larvae, we sub-sampled 10,000 input combinations while still exhaustively iterate through all output neurons. All simulations were run for $T = 50$ time steps, a duration long enough for the network dynamics to stabilize when single input neurons were initially activated.

We also performed a smaller set of connectedness-dependent E-I sampling but with the same coverage on E-I ratio and differential connectedness. Specifically, we sampled from 235 different connectedness-dependent probability vectors, covering uniform (0.1, 0.2, 0.3, 0.5, 0.7, 0.8, 0.9), exponential (28 probability vectors), and non-monotonic relationships (200 probability vectors).

Sparse network training All networks are trained with stochastic gradient descent on Fashion-MNIST with 7000 training examples and 10,000 validation examples. The learning rate and batch size are selected based on grid search and chosen based on the best average across all scenarios. The sparsification and signs are initialized based on settings specified in Table 2. During training, the wiring and E-I identity of each connection is allowed to be updated in classical pruning only, for all other 3 scenarios following Dale's rule, the zero mask and signs are

fixed throughout training.

E-I scenario as in Figure 5	E(E+I)	Exc sparsity	Inhib sparsity	Overall sparsity	$(w_{>0})/(w_{>0} + w_{<0})$
80% Exc (Dale's)	0.8	0.99375	0.975	0.99	0.5
50% Exc (Dale's)	0.5	0.99	0.99	0.99	0.5
20% Exc (Dale's)	0.2	0.975	0.99375	0.99	0.5
classical pruning	N/A	0.99	0.99	0.99	0.5

Table 2: **Sparse network E-I configuration specifications across scenarios.** (related to Figure 5)

Acknowledgements

This work was supported by NSF NeuroNex Award (Grant no. 2014862) (to J.V.), NSF CAREER Award (Grant no. 1942963) (to J.V.), the JHU MINDS Fellowship (to Q.W.), and the Francis Crick Institute core funding (to M.W.), including Cancer Research UK (CC2252), the UK Medical Research Council (CC2252), and the Wellcome Trust (CC2252).

Author contributions

Conceptualization: Q.W.,C.E.P.,and J.T.V. Methodology: Q.W. and C.E.P. Analysis: Q.W. DNN training: Q.W. Larva *Drosophila* neurotransmitter prediction: N.R., Y.Y., C.S., A.S., M.W., A.C., and M.Z. Supervision: C.E.P. and J.T.V. Writing - original draft: Q.W. Writing - Review and editing: Q.W., J.T.V., C.E.P., M.W., M.Z., and A.C.

References and Notes

[1] Joshua T. Vogelstein, Eric W. Bridgeford, Benjamin D. Pedigo, Jaewon Chung, Keith Levin, Brett Mensh, and Carey E. Priebe. Connectal coding: discovering the structures linking cognitive phenotypes to individual histories. *Current Opinion in Neurobiology*, 55:199–212, 2019. ISSN 18736882. doi: 10.1016/j.conb.2019.04.005. URL https://doi.org/10.1016/j.conb.2019.04.005. 1

[2] Patrick Rubin-Delanchy, Joshua Cape, Minh Tang, and Carey E. Priebe. A statistical interpretation of spectral embedding: The generalised random dot product graph. *Journal of the Royal Statistical Society. Series B: Statistical Methodology*, 84(4), 2022. ISSN 14679868. doi: 10.1111/rssb.12509. 1

[3] Michael Winding, Benjamin D. Pedigo, Christopher L. Barnes, Heather G. Patsolic, Youngser Park, Tom Kazimiers, Akira Fushiki, Ingrid V. Andrade, Avinash Khandelwal, Javier Valdes-Aleman, Feng Li, Nadine Randel, Elizabeth Barsotti, Ana Correia, Richard D. Fetter, Volker Hartenstein, Carey E. Priebe, Joshua T. Vogelstein, Albert Cardona, and Marta Zlatic. The connectome of an insect brain. *Science*, 379(6636), 2023. ISSN 10959203. doi: 10.1126/science.add9330. 1, 2, 10, 12

[4] Sven Dorkenwald, Arie Matsliah, Amy R Sterling, Philipp Schlegel, Szi-chieh Yu, Claire E McKellar, Albert Lin, Marta Costa, Katharina Eichler, Yijie Yin, Will Silversmith, Casey Schneider-Mizell, Chris S Jordan, Derrick Brittain, Akhilesh Halageri, Kai Kuehner, Oluwaseun Ogedengbe, Ryan Morey, Jay Gager, Krzysztof Kruk, Eric Perlman, Runzhe Yang, David Deutsch, Doug Bland, Marissa Sorek, Ran Lu, Thomas Macrina, Kisuk Lee, J Alexander Bae, Shang Mu, Barak Nehoran, Eric Mitchell, Sergiy Popovych, Jingpeng Wu, Zhen Jia, Manuel A Castro, Nico Kemnitz, Dodam Ih, Alexander Shakeel Bates, Nils Eckstein, Jan Funke, Forrest Collman, Davi D Bock, Gregory S X E Jefferis, H Sebastian Seung, Mala Murthy, Zairene Lenizo, Austin T Burke, Kyle Patrick Willie, Nikitas Serafetinidis, Nashra Hadjerol, Ryan Willie, Ben Silverman, John Anthony Ocho, Joshua Bañez, Rey Adrian Candilada, Anne Kristiansen, Nelsie Panes, Arti Yadav, Remer Tancontian, Shirleyjoy Serona, Jet Ivan Dolorosa, Kendrick Joules Vinson, Dustin Garner, Regine Salem, Ariel Dagohoy, Jaime Skelton, Mendell Lopez, Laia Serratosa Capdevila, Griffin Badalamente, Thomas Stocks, Anjali Pandey, Darrel Jay Akiatan, James Hebditch, Celia David, Dharini Sapkal, Shaina Mae Monungolh, Varun Sane, Mark Lloyd Pielago, Miguel Albero, Jacquilyn Laude, Márcia dos Santos, Zeba Vohra, Kaiyu Wang, Allien Mae Gogo, Emil Kind, Alvin Josh Mandahay, Chereb Martinez, John David Asis, Chitra Nair, Dhwani Patel,

Marchan Manaytay, Imaan F M Tamimi, Clyde Angelo Lim, Philip Lenard Ampo, Michelle Darapan Pantujan, Alexandre Javier, Daril Bautista, Rashmita Rana, Jansen Seguido, Bhargavi Parmar, John Clyde Saguimpa, Merlin Moore, Markus William Pleijzier, Mark Larson, Joseph Hsu, Itisha Joshi, Dhara Kakadiya, Amalia Braun, Cathy Pilapil, Marina Gkantia, Kaushik Parmar, Quinn Vanderbeck, Irene Salgarella, Christopher Dunne, Eva Munnelly, Chan Hyuk Kang, Lena Lörsch, Jinmook Lee, Lucia Kmecova, Gizem Sancer, Christa Baker, Jenna Joroff, Steven Calle, Yashvi Patel, Olivia Sato, Siqi Fang, Janice Salocot, Farzaan Salman, Sebastian Molina-Obando, Paul Brooks, Mai Bui, Matthew Lichtenberger, Edward Tamboboy, Katie Molloy, Alexis E Santana-Cruz, Anthony Hernandez, Seongbong Yu, Arzoo Diwan, Monika Patel, Travis R Aiken, Sarah Morejohn, Sanna Koskela, Tansy Yang, Daniel Lehmann, Jonas Chojetzki, Sangeeta Sisodiya, Selden Koolman, Philip K Shiu, Sky Cho, Annika Bast, Brian Reicher, Marlon Blanquart, Lucy Houghton, Hyungjun Choi, Maria Ioannidou, Matt Collie, Joanna Eckhardt, Benjamin Gorko, Li Guo, Zhihao Zheng, Alisa Poh, Marina Lin, István Taisz, Wes Murfin, Alvaro Sanz Diez, Nils Reinhard, Peter Gibb, Nidhi Patel, Sandeep Kumar, Minsik Yun, Megan Wang, Devon Jones, Lucas Encarnacion-Rivera, Annalena Oswald, Akanksha Jadia, Mert Erginkaya, Nik Drummond, Leonie Walter, Ibrahim Tastekin, Xin Zhong, Yuta Mabuchi, Fernando J Figueroa Santiago, Urja Verma, Nick Byrne, Edda Kunze, Thomas Crahan, Ryan Margossian, Haein Kim, Iliyan Georgiev, Fabianna Szorenyi, Atsuko Adachi, Benjamin Bargeron, Tomke Stürner, Damian Demarest, Burak Gür, Andrea N Becker, Robert Turnbull, Ashley Morren, Andrea Sandoval, Anthony Moreno-Sanchez, Diego A Pacheco, Eleni Samara, Haley Croke, Alexander Thomson, Connor Laughland, Suchetana B Dutta, Paula Guiomar Alarcón de Antón, Binglin Huang, Patricia Pujols, Isabel Haber, Amanda González-Segarra, Daniel T Choe, Veronika Lukyanova, Nino Mancini, Zequan Liu, Tatsuo Okubo, Miriam A Flynn, Gianna Vitelli, Meghan Laturney, Feng Li, Shuo Cao, Carolina Manyari-Diaz, Hyunsoo Yim, Anh Duc Le, Kate Maier, Seungyun Yu, Yeonju Nam, Daniel Bąba, Amanda Abusaif, Audrey Francis, Jesse Gayk, Sommer S Huntress, Raquel Barajas, Mindy Kim, Xinyue Cui, Gabriella R Sterne, Anna Li, Keehyun Park, Georgia Dempsey, Alan Mathew, Jinseong Kim, Taewan Kim, Guan-ting Wu, Serene Dhawan, Margarida Brotas, Cheng-hao Zhang, Shanice Bailey, Alexander Del Toro, Runzhe Yang, Stephan Gerhard, Andrew Champion, David J Anderson, Rudy Behnia, Salil S Bidaye, Alexander Borst, Eugenia Chiappe, Kenneth J Colodner, Andrew Dacks, Barry Dickson, Denise Garcia, Stefanie Hampel, Volker Hartenstein, Bassem Hassan, Charlotte Helfrich-Forster, Wolf Huetteroth, Jinseop Kim, Sung Soo Kim, Young-Joon Kim, Jae Young Kwon, Wei-Chung Lee, Gerit A Linneweber, Gaby Maimon, Richard Mann, Stéphane Noselli, Michael Pankratz, Lucia Prieto-Godino, Jenny Read, Michael Reiser, Katie von Reyn, Carlos Ribeiro, Kristin Scott, Andrew M Seeds, Mareike Selcho, Marion Silies, Julie Simpson, Scott Waddell, Mathias F Wernet, Rachel I Wilson, Fred W Wolf, Zepeng Yao, Nilay Yapici, Meet Zandawala, and The FlyWire Consortium. Neuronal wiring diagram of an adult brain. *Nature*, 634(8032):124–138, 2024. ISSN 1476-4687. doi: 10.1038/s41586-024-07558-y. URL https://doi.org/10.1038/s41586-024-07558-y. 1, 7, 11, 13

[5] Philipp Schlegel, Yijie Yin, Alexander S Bates, Sven Dorkenwald, Katharina Eichler, Paul Brooks, Daniel S Han, Marina Gkantia, Marcia dos Santos, Eva J Munnelly, Griffin Badalamente, Laia Serratosa Capdevila, Varun A Sane, Alexandra M C Fragniere, Ladann Kiassat, Markus W Pleijzier, Tomke Stürner, Imaan F M Tamimi, Christopher R Dunne, Irene Salgarella, Alexandre Javier, Siqi Fang, Eric Perlman, Tom Kazimiers, Sridhar R Jagannathan, Arie Matsliah, Amy R Sterling, Szi-chieh Yu, Claire E McKellar, Krzysztof Kruk, Doug Bland, Zairene Lenizo, Austin T Burke, Kyle Patrick Willie, Alexander S Bates, Nikitas Serafetinidis, Nashra Hadjerol, Ryan Willie, Ben Silverman, John Anthony Ocho, Joshua Bañez, Rey Adrian Candilada, Jay Gager, Anne Kristiansen, Nelsie Panes, Arti Yadav, Remer Tancontian, Shirleyjoy Serona, Jet Ivan Dolorosa, Kendrick Joules Vinson, Dustin Garner, Regine Salem, Ariel Dagohoy, Jaime Skelton, Mendell Lopez, Thomas Stocks, Anjali Pandey, Darrel Jay Akiatan, James Hebditch, Celia David, Dharini Sapkal, Shaina Mae Monungolh, Varun Sane, Mark Lloyd Pielago, Miguel Albero, Jacquilyn Laude, Márcia dos Santos, David Deutsch, Zeba Vohra, Kaiyu Wang, Allien Mae Gogo, Emil Kind, Alvin Josh Mandahay, Chereb Martinez, John David Asis, Chitra Nair, Dhwani Patel, Marchan Manaytay, Clyde Angelo Lim, Philip Lenard Ampo, Michelle Darapan Pantujan, Daril Bautista, Rashmita Rana, Jansen Seguido, Bhargavi Parmar, John Clyde Saguimpa, Merlin Moore, Markus W Pleijzier, Mark Larson, Joseph Hsu, Itisha Joshi, Dhara Kakadiya, Amalia Braun, Cathy Pilapil, Kaushik Parmar, Quinn Vanderbeck, Christopher Dunne, Eva Munnelly, Chan Hyuk Kang, Lena Lörsch, Jinmook Lee, Lucia Kmecova, Gizem Sancer, Christa Baker, Jenna Joroff, Steven Calle, Yashvi Patel, Olivia Sato, Janice Salocot, Farzaan Salman, Sebastian Molina-Obando, Mai Bui, Matthew Lichtenberger, Edmark Tamboboy, Katie Molloy, Alexis E Santana-Cruz, Anthony Hernandez, Seongbong Yu,

Marissa Sorek, Arzoo Diwan, Monika Patel, Travis R Aiken, Sarah Morejohn, Sanna Koskela, Tansy Yang, Daniel Lehmann, Jonas Chojetzki, Sangeeta Sisodiya, Selden Koolman, Philip K Shiu, Sky Cho, Annika Bast, Brian Reicher, Marlon Blanquart, Lucy Houghton, Hyungjun Choi, Maria Ioannidou, Matt Collie, Joanna Eckhardt, Benjamin Gorko, Li Guo, Zhihao Zheng, Alisa Poh, Marina Lin, István Taisz, Wes Murfin, Álvaro Sanz Díez, Nils Reinhard, Peter Gibb, Nidhi Patel, Sandeep Kumar, Minsik Yun, Megan Wang, Devon Jones, Lucas Encarnacion-Rivera, Annalena Oswald, Akanksha Jadia, Mert Erginkaya, Nik Drummond, Leonie Walter, Ibrahim Tastekin, Xin Zhong, Yuta Mabuchi, Fernando J Figueroa Santiago, Urja Verma, Nick Byrne, Edda Kunze, Thomas Crahan, Ryan Margossian, Haein Kim, Iliyan Georgiev, Fabianna Szorenyi, Atsuko Adachi, Benjamin Bargeron, Tomke Stürner, Damian Demarest, Burak Gür, Andrea N Becker, Robert Turnbull, Ashley Morren, Andrea Sandoval, Anthony Moreno-Sanchez, Diego A Pacheco, Eleni Samara, Haley Croke, Alexander Thomson, Connor Laughland, Suchetana B Dutta, Paula Guiomar Alarcón de Antón, Binglin Huang, Patricia Pujols, Isabel Haber, Amanda González-Segarra, Albert Lin, Daniel T Choe, Veronika Lukyanova, Nino Mancini, Zequan Liu, Tatsuo Okubo, Miriam A Flynn, Gianna Vitelli, Meghan Laturney, Feng Li, Shuo Cao, Carolina Manyari-Diaz, Hyunsoo Yim, Anh Duc Le, Kate Maier, Seungyun Yu, Yeonju Nam, Daniel Bąba, Amanda Abusaif, Audrey Francis, Jesse Gayk, Sommer S Huntress, Raquel Barajas, Mindy Kim, Xinyue Cui, Amy R Sterling, Gabriella R Sterne, Anna Li, Keehyun Park, Georgia Dempsey, Alan Mathew, Jinseong Kim, Taewan Kim, Guan-ting Wu, Serene Dhawan, Margarida Brotas, Cheng-hao Zhang, Shanice Bailey, Alexander Del Toro, Kisuk Lee, Thomas Macrina, Casey Schneider-Mizell, Sergiy Popovych, Oluwaseun Ogedengbe, Runzhe Yang, Akhilesh Halageri, Will Silversmith, Stephan Gerhard, Andrew Champion, Nils Eckstein, Dodam Ih, Nico Kemnitz, Manuel Castro, Zhen Jia, Jingpeng Wu, Eric Mitchell, Barak Nehoran, Shang Mu, J Alexander Bae, Ran Lu, Ryan Morey, Kai Kuehner, Derrick Brittain, Chris S Jordan, David J Anderson, Rudy Behnia, Salil S Bidaye, Alexander Borst, Eugenia Chiappe, Forrest Collman, Kenneth J Colodner, Andrew Dacks, Barry Dickson, Jan Funke, Denise Garcia, Stefanie Hampel, Volker Hartenstein, Bassem Hassan, Charlotte Helfrich-Forster, Wolf Huetteroth, Jinseop Kim, Sung Soo Kim, Young-Joon Kim, Jae Young Kwon, Wei-Chung Lee, Gerit A Linneweber, Gaby Maimon, Richard Mann, Stéphane Noselli, Michael Pankratz, Lucia Prieto-Godino, Jenny Read, Michael Reiser, Katie von Reyn, Carlos Ribeiro, Kristin Scott, Andrew M Seeds, Mareike Selcho, Marion Silies, Julie Simpson, Scott Waddell, Mathias F Wernet, Rachel I Wilson, Fred W Wolf, Zepeng Yao, Nilay Yapici, and FlyWire Consortium. Whole-brain annotation and multi-connectome cell typing of Drosophila. *Nature*, 634(8032):139–152, 2024. ISSN 1476-4687. doi: 10.1038/s41586-024-07686-5. URL https://doi.org/10.1038/s41586-024-07686-5.

[6] Davi D. Bock, Wei Chung Allen Lee, Aaron M. Kerlin, Mark L. Andermann, Greg Hood, Arthur W. Wetzel, Sergey Yurgenson, Edward R. Soucy, Hyon Suk Kim, and R. Clay Reid. Network anatomy and in vivo physiology of visual cortical neurons. *Nature*, 471(7337):177–184, 2011. ISSN 00280836. doi: 10.1038/nature09802. URL http://dx.doi.org/10.1038/nature09802.

[7] David Grant Colburn Hildebrand, Marcelo Cicconet, Russel Miguel Torres, Woohyuk Choi, Tran Minh Quan, Jungmin Moon, Arthur Willis Wetzel, Andrew Scott Champion, Brett Jesse Graham, Owen Randlett, George Scott Plummer, Ruben Portugues, Isaac Henry Bianco, Stephan Saalfeld, Alexander David Baden, Kunal Lillaney, Randal Burns, Joshua Tzvi Vogelstein, Alexander Franz Schier, Wei Chung Allen Lee, Won Ki Jeong, Jeff William Lichtman, and Florian Engert. Whole-brain serial-section electron microscopy in larval zebrafish. *Nature*, 545(7654), 2017. ISSN 14764687. doi: 10.1038/nature22356. 12

[8] Fabian Svara, Dominique Förster, Fumi Kubo, Michał Januszewski, Marco dal Maschio, Philipp J. Schubert, Jörgen Kornfeld, Adrian A. Wanner, Eva Laurell, Winfried Denk, and Herwig Baier. Automated synapse-level reconstruction of neural circuits in the larval zebrafish brain. *Nature Methods*, 19(11), 2022. ISSN 15487105. doi: 10.1038/s41592-022-01621-0.

[9] The MICrONS Consortium, J. Alexander Bae, Mahaly Baptiste, Agnes L. Bodor, Derrick Brittain, JoAnn Buchanan, Daniel J. Bumbarger, Manuel A. Castro, Brendan Celii, Erick Cobos, Forrest Collman, Nuno Maçarico da Costa, Sven Dorkenwald, Leila Elabbady, Paul G. Fahey, Tim Fliss, Emmanouil Froudarakis, Jay Gager, Clare Gamlin, Akhilesh Halageri, James Hebditch, Zhen Jia, Chris Jordan, Daniel Kapner, Nico Kemnitz, Sam Kinn, Selden Koolman, Kai Kuehner, Kisuk Lee, Kai Li, Ran Lu, Thomas Macrina, Gayathri Mahalingam, Sarah McReynolds, Elanine Miranda, Eric Mitchell, Shanka Subhra Mondal, Merlin Moore, Shang Mu, Taliah Muhammad, Barak Nehoran, Oluwaseun Ogedengbe, Christos Papadopoulos, Stelios Papadopoulos, Saumil Patel, Xaq Pitkow, Sergiy Popovych, Anthony Ramos, R. Clay Reid, Jacob Reimer,

Casey M. Schneider-Mizell, H. Sebastian Seung, Ben Silverman, William Silversmith, Amy Sterling, Fabian H. Sinz, Cameron L. Smith, Shelby Suckow, Marc Takeno, Zheng H. Tan, Andreas S. Tolias, Russel Torres, Nicholas L. Turner, Edgar Y. Walker, Tianyu Wang, Grace Williams, Sarah Williams, Kyle Willie, Ryan Willie, William Wong, Jingpeng Wu, Chris Xu, Runzhe Yang, Dimitri Yatsenko, Fei Ye, Wenjing Yin, and Szi-chieh Yu. Functional connectomics spanning multiple areas of mouse visual cortex. *bioRxiv*, 2021.

[10] Alexander Shapson-Coe, Michał Januszewski, Daniel R Berger, Art Pope, Yuelong Wu, Tim Blakely, Richard L Schalek, Peter H Li, Shuohong Wang, Jeremy Maitin-Shepard, Neha Karlupia, Sven Dorkenwald, Evelina Sjostedt, Laramie Leavitt, Dongil Lee, Jakob Troidl, Forrest Collman, Luke Bailey, Angerica Fitzmaurice, Rohin Kar, Benjamin Field, Hank Wu, Julian Wagner-Carena, David Aley, Joanna Lau, Zudi Lin, Donglai Wei, Hanspeter Pfister, Adi Peleg, Viren Jain, and Jeff W Lichtman. A petavoxel fragment of human cerebral cortex reconstructed at nanoscale resolution. *Science*, 384(6696):eadk4858, 2024. doi: 10.1126/science.adk4858. URL https://www.science.org/doi/abs/10.1126/science.adk4858.

[11] Narayanan Kasthuri, Kenneth Jeffrey Hayworth, Daniel Raimund Berger, Richard Lee Schalek, José Angel Conchello, Seymour Knowles-Barley, Dongil Lee, Amelio Vázquez-Reina, Verena Kaynig, Thouis Raymond Jones, Mike Roberts, Josh Lyskowski Morgan, Juan Carlos Tapia, H. Sebastian Seung, William Gray Roncal, Joshua Tzvi Vogelstein, Randal Burns, Daniel Lewis Sussman, Carey Eldin Priebe, Hanspeter Pfister, and Jeff William Lichtman. Saturated Reconstruction of a Volume of Neocortex. *Cell*, 162(3), 2015. ISSN 10974172. doi: 10.1016/j.cell.2015.06.054. 1, 12

[12] Mehryar Mohri, Afshin Rostamizadeh, and Ameet Talwalkar. *Foundations of Machine Learning*. The MIT Press, 2012. ISBN 026201825X. 1

[13] Marc Corrales, Benjamin T. Cocanougher, Andrea B. Kohn, Jason D. Wittenbach, Xi S. Long, Andrew Lemire, Albert Cardona, Robert H. Singer, Leonid L. Moroz, and Marta Zlatic. A single-cell transcriptomic atlas of complete insect nervous systems across multiple life stages. *Neural Development*, 17(1), 2022. ISSN 17498104. doi: 10.1186/s13064-022-00164-6. 1, 3, 5, 7, 11, 13

[14] Viktória K. Vereczki, Kinga Müller, Éva Krizsán, Zoltán Máté, Zsuzsanna Fekete, Laura Rovira-Esteban, Judit M. Veres, Ferenc Erdélyi, and Norbert Hájos. Total number and ratio of GABAergic neuron types in the mouse lateral and basal amygdala. *Journal of Neuroscience*, 41(21), 2021. ISSN 15292401. doi: 10.1523/JNEUROSCI.2700-20.2021. 1, 11

[15] Daniel Keller, Csaba Erö, and Henry Markram. Cell densities in the mouse brain: A systematic review, 2018. ISSN 16625129. 11

[16] Lydia Ouellet and Etienne de Villers-Sidani. Trajectory of the main GABAergic interneuron populations from early development to old age in the rat primary auditory cortex. *Frontiers in Neuroanatomy*, 8(JUN), 2014. ISSN 16625129. doi: 10.3389/fnana.2014.00040. 11

[17] Clermont Beaulieu. Numerical data on neocortical neurons in adult rat, with special reference to the GABA population. *Brain Research*, 609(1-2), 1993. ISSN 00068993. doi: 10.1016/0006-8993(93)90884-P.

[18] Hanno S. Meyer, Daniel Schwarz, Verena C. Wimmer, Arno C. Schmitt, Jason N.D. Kerr, Bert Sakmann, and Moritz Helmstaedter. Inhibitory interneurons in a cortical column form hot zones of inhibition in layers 2 and 5A. *Proceedings of the National Academy of Sciences of the United States of America*, 108(40), 2011. ISSN 00278424. doi: 10.1073/pnas.1113648108. 11

[19] Y. Aika, J. Q. Ren, K. Kosaka, and T. Kosaka. Quantitative analysis of GABA-like-immunoreactive and parvalbumin-containing neurons in the CA1 region of the rat hippocampus using a stereological method, the disector. *Experimental Brain Research*, 99(2), 1994. ISSN 00144819. doi: 10.1007/BF00239593. 11

[20] Walter Woodson, Liliana Nitecka, and Yehezkel Ben-Ari. Organization of the GABAergic system in the rat hippocampal formation: A quantitative immunocytochemical study. *Journal of Comparative Neurology*, 280 (2), 1989. ISSN 10969861. doi: 10.1002/cne.902800207. 1, 11

[21] P. L.A. Gabbott and P. Somogyi. Quantitative distribution of GABA-immunoreactive neurons in the visual cortex (area 17) of the cat. *Experimental Brain Research*, 61(2), 1986. ISSN 00144819. doi: 10.1007/BF00239522. 1, 11

[22] Jianying Li and Harris D. Schwark. Distribution and proportions of GABA-Immunoreactive neurons in cat primary somatosensory cortex. *Journal of Comparative Neurology*, 343(3), 1994. ISSN 10969861. doi: 10.1002/cne.903430302.

[23] Jorge J. Prieto, Barbara A. Peterson, and Jeffery A. Winer. Morphology and spatial distribution of GABAergic neurons in cat primary auditory cortex (AI). *Journal of Comparative Neurology*, 344(3), 1994. ISSN 10969861. doi: 10.1002/cne.903440304. 1, 11

[24] S. H. Hendry, H. D. Schwark, E. G. Jones, and J. Yan. Numbers and proportions of GABA-immunoreactive neurons in different areas of monkey cerebral cortex. *The Journal of neuroscience : the official journal of the Society for Neuroscience*, 7(5), 1987. ISSN 02706474. doi: 10.1523/jneurosci.07-05-01503.1987. 1, 11

[25] Jean Pierre Hornung and N. De Tribolet. Distribution of GABA-containing neurons in human frontal cortex: a quantitative immunocytochemical study. *Anatomy and Embryology*, 189(2), 1994. ISSN 03402061. doi: 10.1007/BF00185772. 1, 11

[26] Britt Anderson, Jessie J. Peissig, Jedediah Singer, and David L. Sheinberg. XOR style tasks for testing visual object processing in monkeys. *Vision Research*, 46(11), 2006. ISSN 00426989. doi: 10.1016/j.visres.2005.11.023. 2

[27] J David Smith, John Paul Minda, and David A Washburn. Category learning in rhesus monkeys: a study of the Shepard, Hovland, and Jenkins (1961) tasks. *Journal of Experimental Psychology: General*, 133(3):398, 2004.

[28] Chris I Baker, Marlene Behrmann, and Carl R Olson. Impact of learning on representation of parts and wholes in monkey inferotemporal cortex. *Nature neuroscience*, 5(11):1210–1216, 2002.

[29] S J Thorpe, K O'Regan, and A Pouget. Humans fail on XOR pattern classification problems. *Neural networks from models to applications*, pages 12–25, 1989. 2

[30] Marvin Minsky and Seymour Papert. *Perceptrons.* M.I.T. Press, Oxford, England, 1969. 2

[31] Kurt Hornik, Maxwell Stinchcombe, and Halbert White. Multilayer feedforward networks are universal approximators. *Neural Networks*, 2(5):359–366, 1 1989. ISSN 0893-6080. doi: 10.1016/0893-6080(89)90020-8. 2

[32] G. Cybenko. Approximation by superpositions of a sigmoidal function. *Mathematics of Control, Signals and Systems 1989 2:4*, 2(4):303–314, 12 1989. ISSN 1435-568X. doi: 10.1007/BF02551274. URL https://link.springer.com/article/10.1007/BF02551274.

[33] Kurt Hornik. Approximation capabilities of multilayer feedforward networks. *Neural Networks*, 4(2):251–257, 1 1991. ISSN 08936080. doi: 10.1016/0893-6080(91)90009-T. URL https://linkinghub.elsevier.com/retrieve/pii/089360809190009T. 2

[34] Qingyang Wang, Mike A Powell, Ali Geisa, Eric Bridgeford, Carey E Priebe, and Joshua T Vogelstein. Why do networks have inhibitory/negative connections? In *Proceedings of the IEEE/CVF International Conference on Computer Vision (ICCV)*, pages 22551–22559, 10 2023. 2, 3

[35] Sonja B. Hofer, Ho Ko, Bruno Pichler, Joshua Vogelstein, Hana Ros, Hongkui Zeng, Ed Lein, Nicholas A. Lesica, and Thomas D. Mrsic-Flogel. Differential connectivity and response dynamics of excitatory and inhibitory neurons in visual cortex. *Nature Neuroscience*, 14(8), 2011. ISSN 10976256. doi: 10.1038/nn.2876. 4

[36] Aaron M. Kerlin, Mark L. Andermann, Vladimir K. Berezovskii, and R. Clay Reid. Broadly Tuned Response Properties of Diverse Inhibitory Neuron Subtypes in Mouse Visual Cortex. *Neuron*, 67(5), 2010. ISSN 08966273. doi: 10.1016/j.neuron.2010.08.002.

[37] Benjamin Scholl, Jagruti J. Pattadkal, Geoffrey A. Dilly, Nicholas J. Priebe, and Boris V. Zemelman. Local Integration Accounts for Weak Selectivity of Mouse Neocortical Parvalbumin Interneurons. *Neuron*, 87(2), 2015. ISSN 10974199. doi: 10.1016/j.neuron.2015.06.030. 4

[38] Adam M. Packer and Rafael Yuste. Dense, unspecific connectivity of neocortical parvalbumin-positive interneurons: A canonical microcircuit for inhibition? *Journal of Neuroscience*, 31(37), 2011. ISSN 02706474. doi: 10.1523/JNEUROSCI.3131-11.2011. 4

[39] Elodie Fino and Rafael Yuste. Dense inhibitory connectivity in neocortex. *Neuron*, 69(6), 2011. ISSN 08966273. doi: 10.1016/j.neuron.2011.02.025. 4

[40] Charles W. Dunnett. A Multiple Comparison Procedure for Comparing Several Treatments with a Control. *Journal of the American Statistical Association*, 50(272), 1955. ISSN 1537274X. doi: 10.1080/01621459.1955.10501294. 5

[41] Nils Eckstein, Alexander Shakeel Bates, Andrew Champion, Michelle Du, Yijie Yin, Philipp Schlegel, Alicia Kun-Yang Lu, Thomson Rymer, Samantha Finley-May, Tyler Paterson, Ruchi Parekh, Sven Dorkenwald, Arie Matsliah, Szi-Chieh Yu, Claire McKellar, Amy Sterling, Katharina Eichler, Marta Costa, Sebastian Seung, Mala Murthy, Volker Hartenstein, Gregory S X E Jefferis, and Jan Funke. Neurotransmitter classification from electron microscopy images at synaptic sites in Drosophila melanogaster. *Cell*, 187(10): 2574–2594, 5 2024. ISSN 0092-8674. doi: 10.1016/j.cell.2024.03.016. URL https://doi.org/10.1016/j.cell.2024.03.016. 5, 13

[42] Kristofer Davie, Jasper Janssens, Duygu Koldere, Maxime De Waegeneer, Uli Pech, Łukasz Kreft, Sara Aibar, Samira Makhzami, Valerie Christiaens, Carmen Bravo González-Blas, Suresh Poovathingal, Gert Hulselmans, Katina I. Spanier, Thomas Moerman, Bram Vanspauwen, Sarah Geurs, Thierry Voet, Jeroen Lammertyn, Bernard Thienpont, Sha Liu, Nikos Konstantinides, Mark Fiers, Patrik Verstreken, and Stein Aerts. A Single-Cell Transcriptome Atlas of the Aging Drosophila Brain. *Cell*, 174(4), 2018. ISSN 10974172. doi: 10.1016/j.cell.2018.05.057. 7, 9, 11

[43] Jonathan Frankle and Michael Carbin. The lottery ticket hypothesis: Finding sparse, trainable neural networks. In *7th International Conference on Learning Representations, ICLR 2019*, 2019. URL https://openreview.net/forum?id=rJl-b3RcF7. 9

[44] Hattie Zhou, Janice Lan, Rosanne Liu, and Jason Yosinski. Deconstructing lottery tickets: Zeros, signs, and the supermask. In *Advances in Neural Information Processing Systems*, volume 32, 2019. 9

[45] Advait Harshal Gadhikar and Rebekka Burkholz. Masks, Signs, And Learning Rate Rewinding. In *The Twelfth International Conference on Learning Representations*, 2024. URL https://openreview.net/forum?id=qODvxQ8TXW. 9

[46] Ran Rubin, L. F. Abbott, and Haim Sompolinsky. Balanced excitation and inhibition are required for high-capacity, noise-robust neuronal selectivity. *Proceedings of the National Academy of Sciences of the United States of America*, 114(44), 2017. ISSN 10916490. doi: 10.1073/pnas.1705841114. 10

[47] Vittorio Capano, Hans J. Herrmann, and Lucilla De Arcangelis. Optimal percentage of inhibitory synapses in multi-task learning. *Scientific Reports*, 5, 2015. ISSN 20452322. doi: 10.1038/srep09895. 10

[48] Ezekiel Williams, Avery Hee-Woon Ryoo, Thomas Jiralerspong, Alexandre Payeur, Matthew G Perich, Luca Mazzucato, and Guillaume Lajoie. Expressivity of Neural Networks with Random Weights and Learned Biases, 2024. URL https://arxiv.org/abs/2407.00957. 10

[49] Qingyang Wang, Michael Alan Powell, Eric W Bridgeford, Ali Geisa, and Joshua T Vogelstein. Polarity Is All You Need to Learn and Transfer Faster. In Andreas Krause, Emma Brunskill, Kyunghyun Cho, Barbara Engelhardt, Sivan Sabato, and Jonathan Scarlett, editors, *Proceedings of the 40th International Conference on Machine Learning*, volume 202 of *Proceedings of Machine Learning Research*, pages 36264–36284. PMLR, 11 2023. URL https://proceedings.mlr.press/v202/wang23ae.html. 10

[50] Sueyeon Chung, Daniel D. Lee, and Haim Sompolinsky. Classification and Geometry of General Perceptual Manifolds. *Physical Review X*, 8(3):1–27, 2018. ISSN 21603308. doi: 10.1103/PhysRevX.8.031003. 11

[51] Uri Cohen, Sue Yeon Chung, Daniel D. Lee, and Haim Sompolinsky. Separability and geometry of object manifolds in deep neural networks. *Nature Communications*, 11(1):1–13, 2020. ISSN 20411723. doi: 10.1038/s41467-020-14578-5. URL http://dx.doi.org/10.1038/s41467-020-14578-5.

[52] Chi-Ning Chou, Luke Arend, Albert J Wakhloo, Royoung Kim, Will Slatton, and SueYeon Chung. Neural Manifold Capacity Captures Representation Geometry, Correlations, and Task-Efficiency Across Species and Behaviors. *bioRxiv*, page 2024.02.26.582157, 1 2024. doi: 10.1101/2024.02.26.582157. URL http://biorxiv.org/content/early/2024/02/28/2024.02.26.582157.abstract.

[53] Francesca Mignacco, Chi-Ning Chou, and SueYeon Chung. Nonlinear classification of neural manifolds with contextual information, 2024. URL https://arxiv.org/abs/2405.06851. 11

[54] V. Koltchinskii. Rademacher penalties and structural risk minimization. *IEEE Transactions on Information Theory*, 47(5), 2001. ISSN 00189448. doi: 10.1109/18.930926. 11

[55] V. N. Vapnik and A. Ya. Chervonenkis. On the Uniform Convergence of Relative Frequencies of Events to Their Probabilities. *Theory of Probability & Its Applications*, 16(2), 1971. ISSN 0040-585X. doi: 10.1137/1116025. 11

[56] Elise C. Croteau-Chonka, Michael S. Clayton, Lalanti Venkatasubramanian, Samuel N. Harris, Benjamin M.W. Jones, Lakshmi Narayan, Michael Winding, Jean Baptiste Masson, Marta Zlatic, and Kristina T. Klein. High-throughput automated methods for classical and operant conditioning of Drosophila larvae, 2022. ISSN 2050084X. 11

[57] Joshua T. Vogelstein, Youngser Park, Tomoko Ohyama, Rex A. Kerr, James W. Truman, Carey E. Priebe, and Marta Zlatic. Discovery of brainwide neural-behavioral maps via multiscale unsupervised structure learning. *Science*, 344(6182):386–392, 2014. ISSN 10959203. doi: 10.1126/science.1250298. 11

[58] Sahil Loomba, Jakob Straehle, Vijayan Gangadharan, Natalie Heike, Abdelrahman Khalifa, Alessandro Motta, Niansheng Ju, Meike Sievers, Jens Gempt, Hanno S. Meyer, and Moritz Helmstaedter. Connectomic comparison of mouse and human cortex. *Science*, 377(6602), 2022. ISSN 10959203. doi: 10.1126/science.abo0924. 12

[59] Xiao Jing Wang. Macroscopic gradients of synaptic excitation and inhibition in the neocortex. *Nature Reviews Neuroscience*, 21(3), 2020. ISSN 14710048. doi: 10.1038/s41583-020-0262-x. 12

A Supplementary Figures

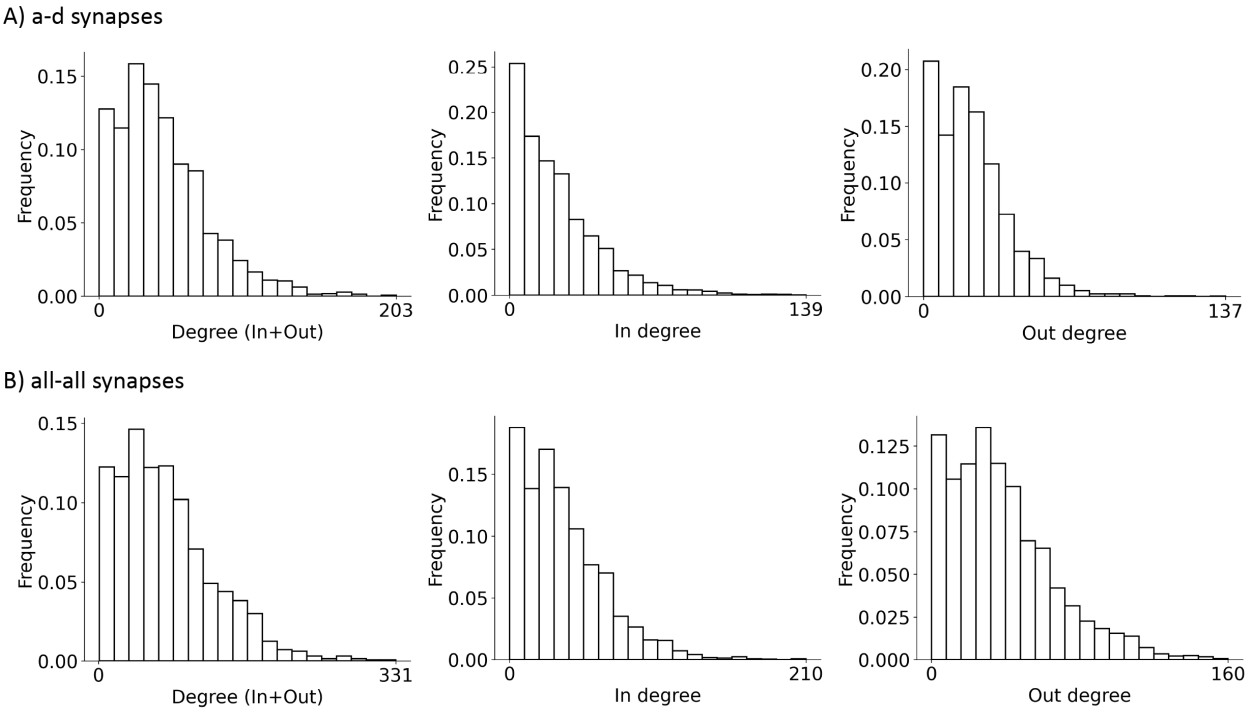

Figure A.1: **The degree distribution of larval *Drosophila* EM connectome.** A) Connections given by axon-dendritic synapses; B) Connections given by all four types of synapses.

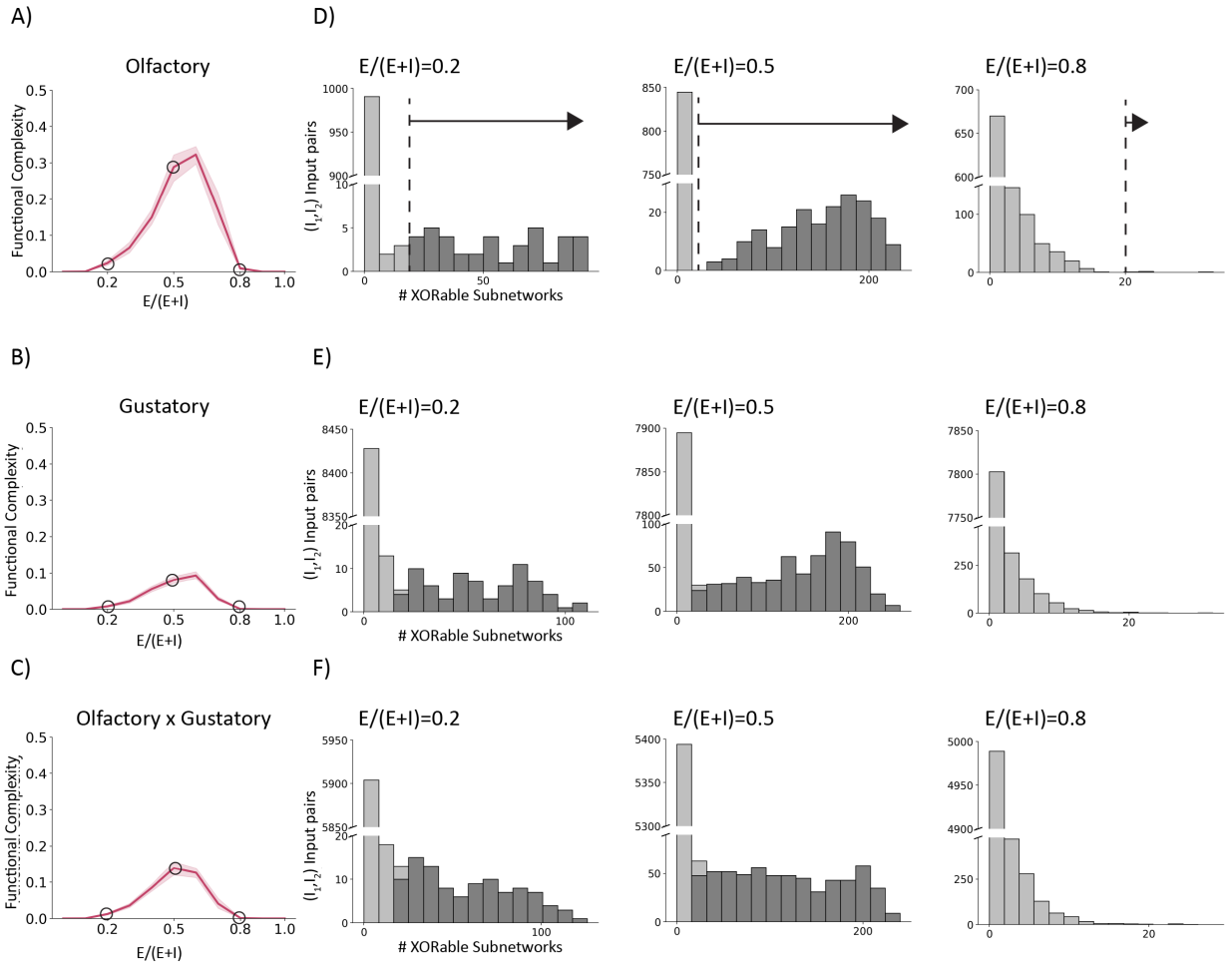

Figure A.2: **Distribution of XORable subnetworks when E-I identities are uniformly sampled across the entire network. (related to Figure 2)** A-C) Functional complexity of networks with different E-I ratios (E-I identities sampled uniformly for all neurons in the EM-constrained RNN). The functional complexities are measured with subnetworks receiving inputs from different sensory modalities, $\{I_1, I_2\} =$: A) $\{\text{Olfactory}_1, \text{Olfactory}_2\}$, B) $\{\text{Gustatory}_1, \text{Gustatory}_2\}$, C) $\{\text{Olfactory}, \text{Gustatory}\}$. Shaded area mark the 95% confidence interval (n=10). Circles mark the corresponding points shown in D-F on the right. D-F) Distributions of XORable subnetworks grouped by the $\{I_1, I_2\}$ input pairs. Each histogram is of a particular sensory modality (given on the left), and of a single RNN with E-I identities sampled at the ratio indicated on top. The functional complexity is then calculated by the fraction of XORable subnetworks, excluding the ones where a unique $\{I_1, I_2\}$ input pair have less than 20 output neurons exhibitng XORable pattern (out of 400 in total) (details in Sec 4). Subnetworks counted towards functional complexity are marked by dark gray.

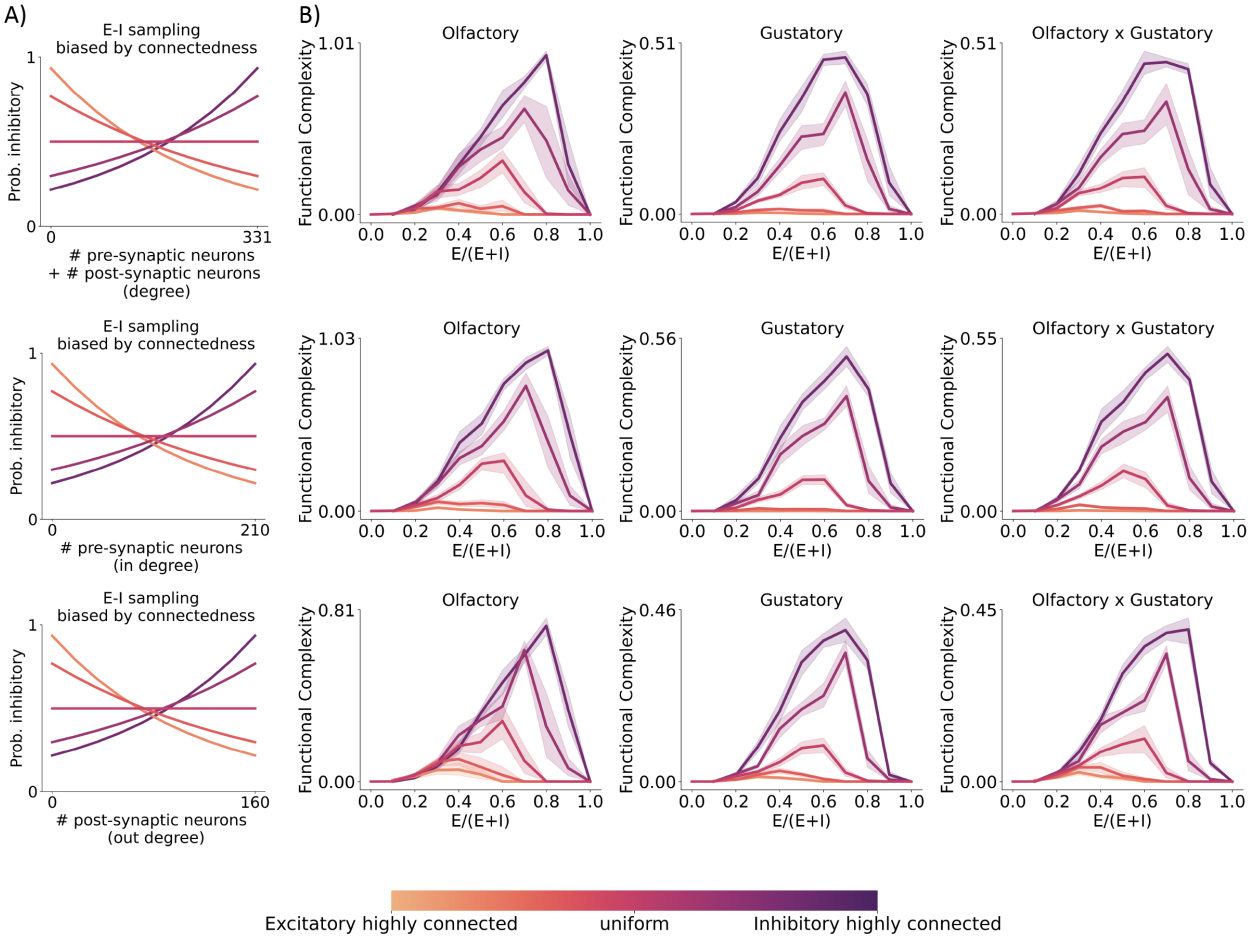

Figure A.3: **Same as Figure 2 except including all-to-all synaptic counts as the EM constraint.**

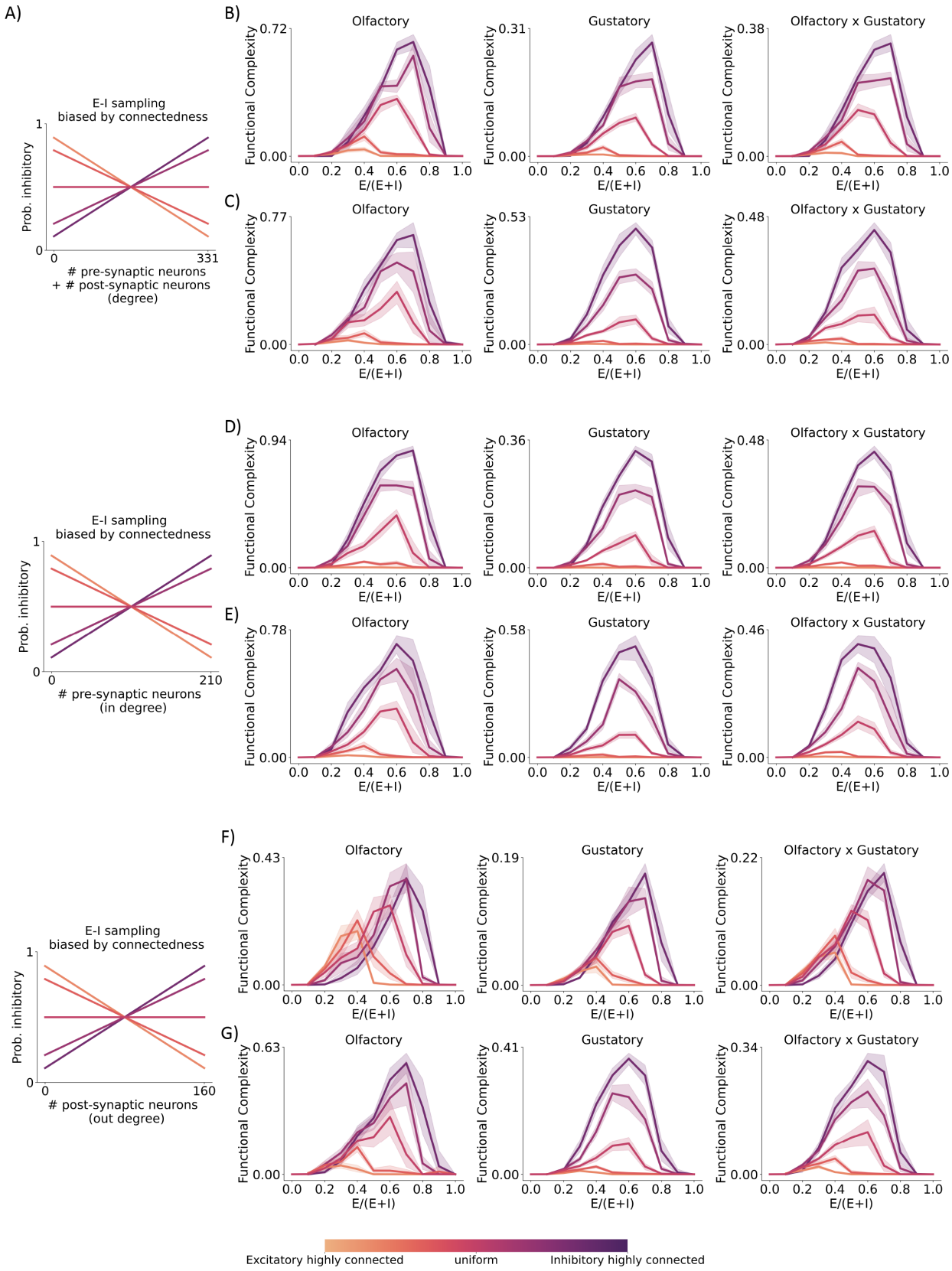

Figure A.4: **Same as Figure 2 except for linear degree-dependent sampling procedures.** A) Linear degree-dependent E-I probability sampling curves. B,D,F) Results for axon-dendrite synapses as the EM constraint. C,E,G) Results for all-to-all synapses as the EM constraint.

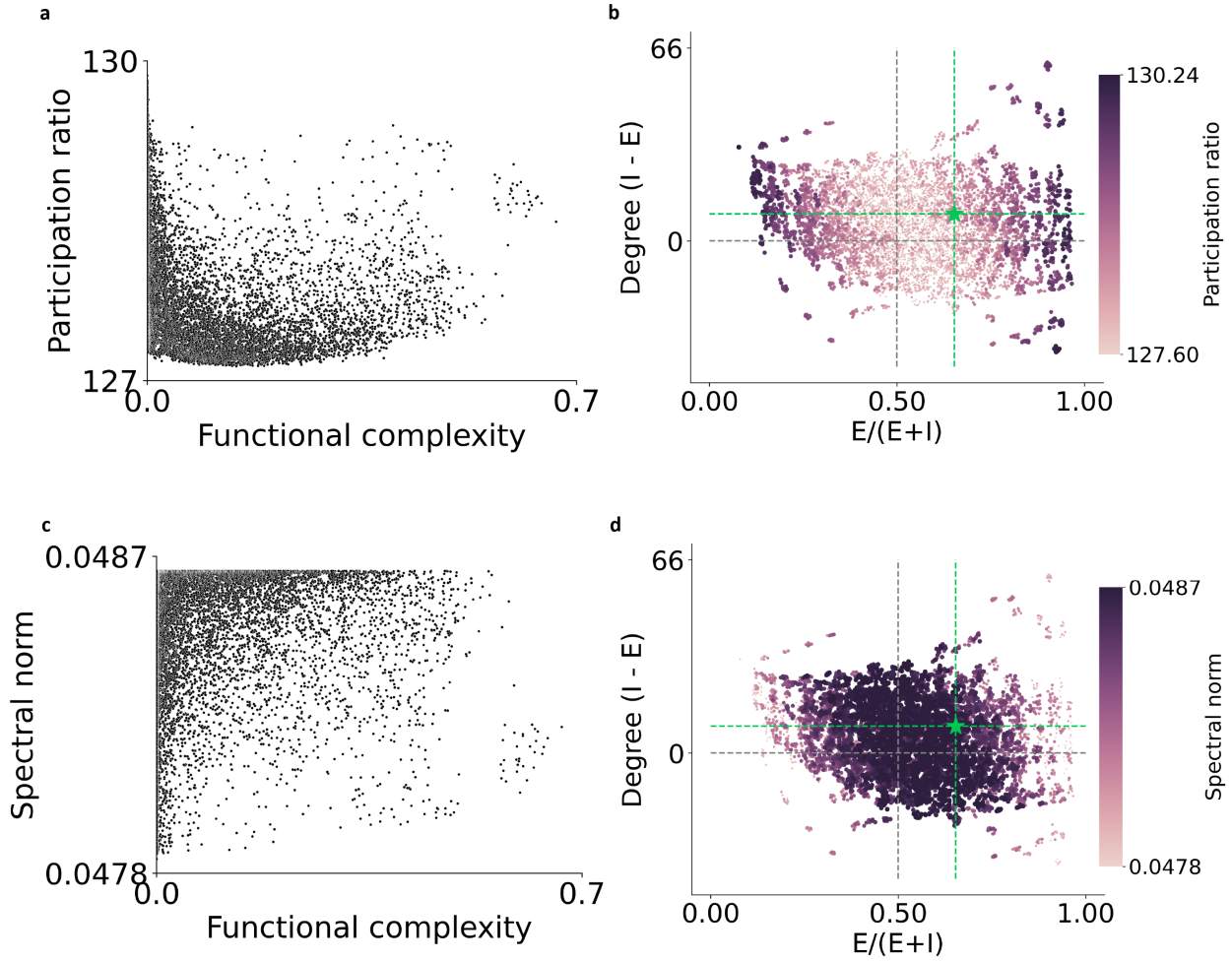

Figure A.5: **Other methods of complexity measurements cannot explain for the network statistics observed in the brain. a**, For all sampled networks based on the larval *Drosophila* EM connectome, we compared its participation ratio, which quantifies the effective dimension of the matrix, to our proposed functional complexity measurement. Evidently, many networks with low functional complexity have a high companion participation ratio. **b**, the high participation ratio networks prefer all excitatory (or inhibitory) compositions and do not show a difference across different degree distributions (y-axis). The high participation ratio networks do not align with the real brain observation (green star). **c**, comparison of our functional complexity measurement to spectral norm which shows little correlation. **d**, the spectral norm of the sampled networks show little variation (notice the small range of the color bar).

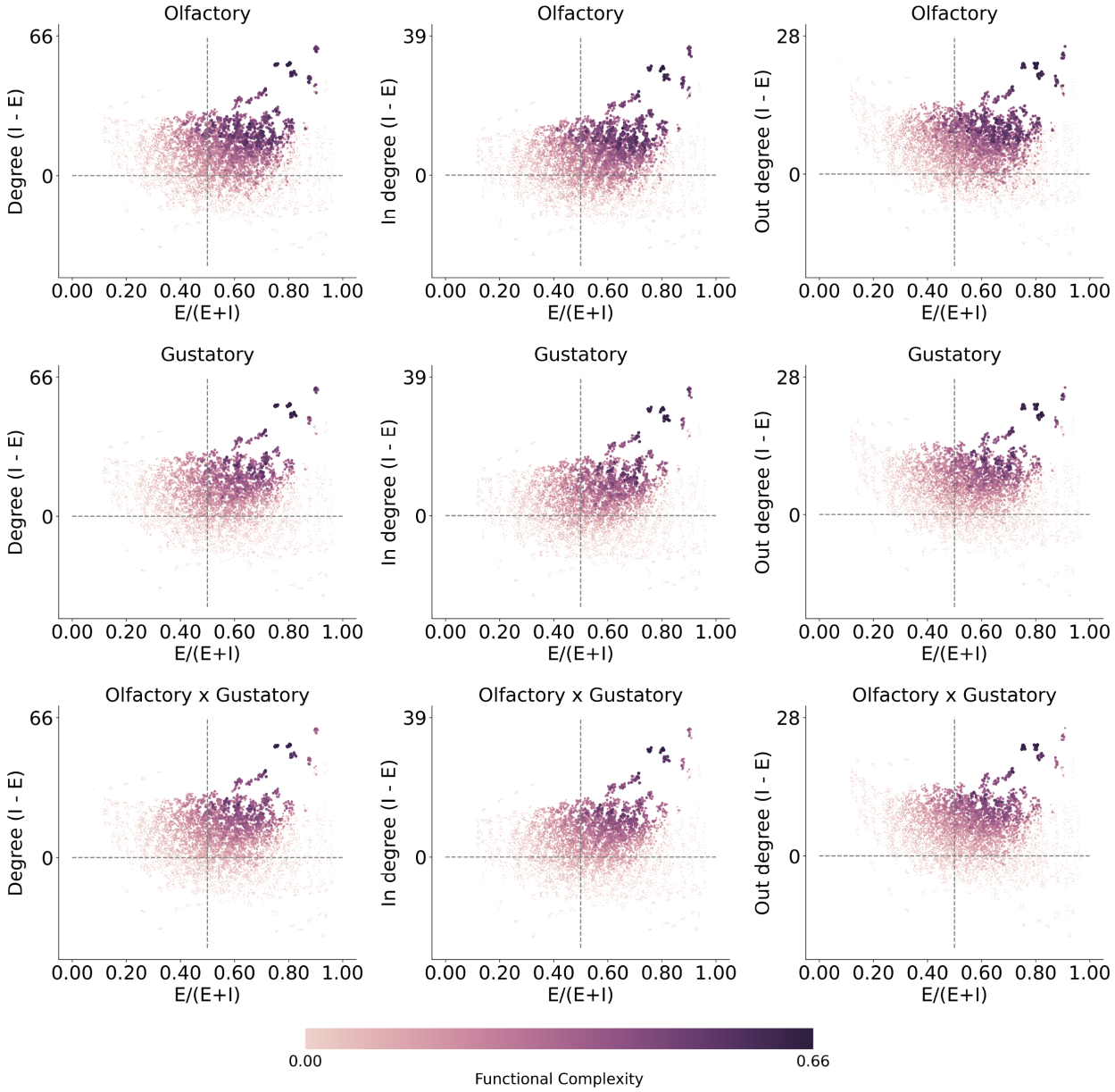

Figure A.6: **Related to Figure 3, functional complexity plotted separately across sensory modalities.** Degree-dependent sampling is based on degree (In+Out). Across sensory modalities (top to bottom) and degree quantification methods (left to right), networks of higher functional complexity (lighter color) have inhibitory neurons more highly connected than excitatory neurons (above horizontal gray line) and there is an over-abundance of excitatory neurons (right to vertical gray line).

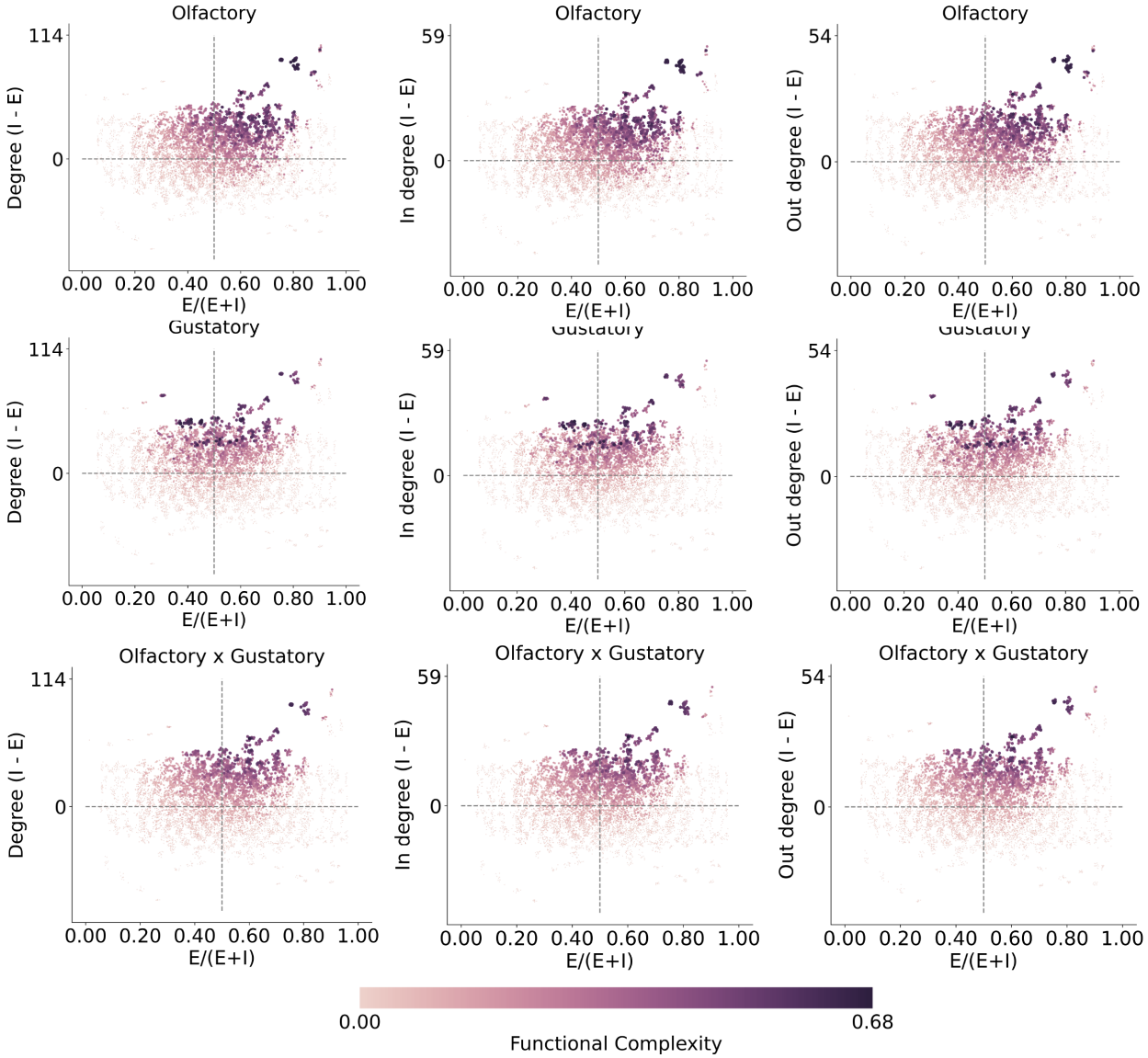

Figure A.7: **Related to Figure 3, functional complexity plotted separately across sensory modalities.** Degree-dependent sampling is based on degree (In+Out) and the connection weight is given by all-all synaptic counts. Across sensory modalities (top to bottom) and degree quantification methods (left to right), networks of higher functional complexity (lighter color) have inhibitory neurons more highly connected than excitatory neurons (above horizontal gray line) and there is an over-abundance of excitatory neurons (right to vertical gray line).

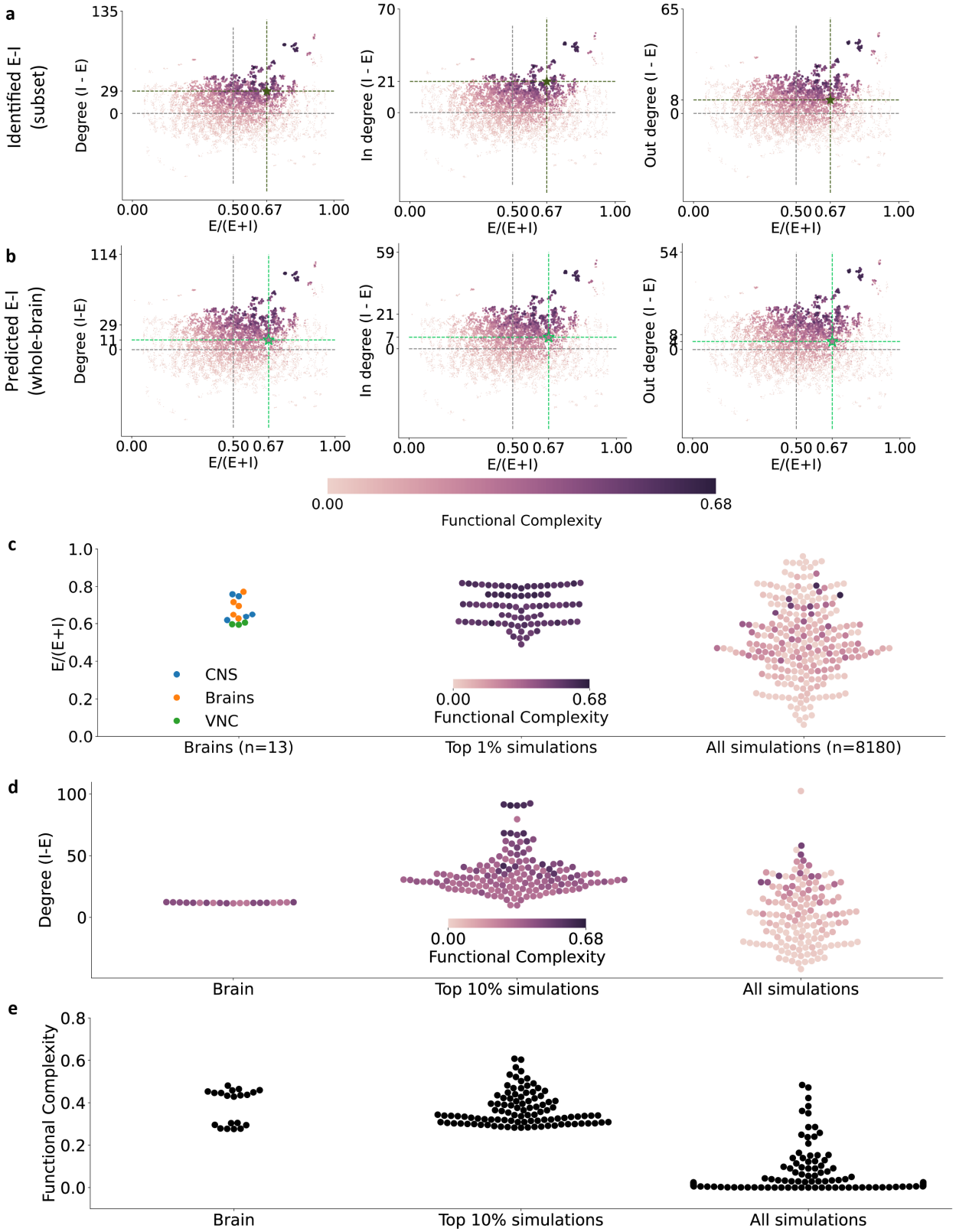

Figure A.8: **Same as Figure 3 except including all-to-all synaptic counts as the EM constraint.** The mean E-I ratio of the top 13 group-averages and top 1% simulations are **not** statistical significantly different from the 13 brain E-I ratios (two-sided two-sample t-test, p-val: 0.99, 0.94 respectively); while the mean of all simulations are statistical significantly different from the brain observations (p-val: 0.01). Multiple comparisons corrected by Dunnett's.

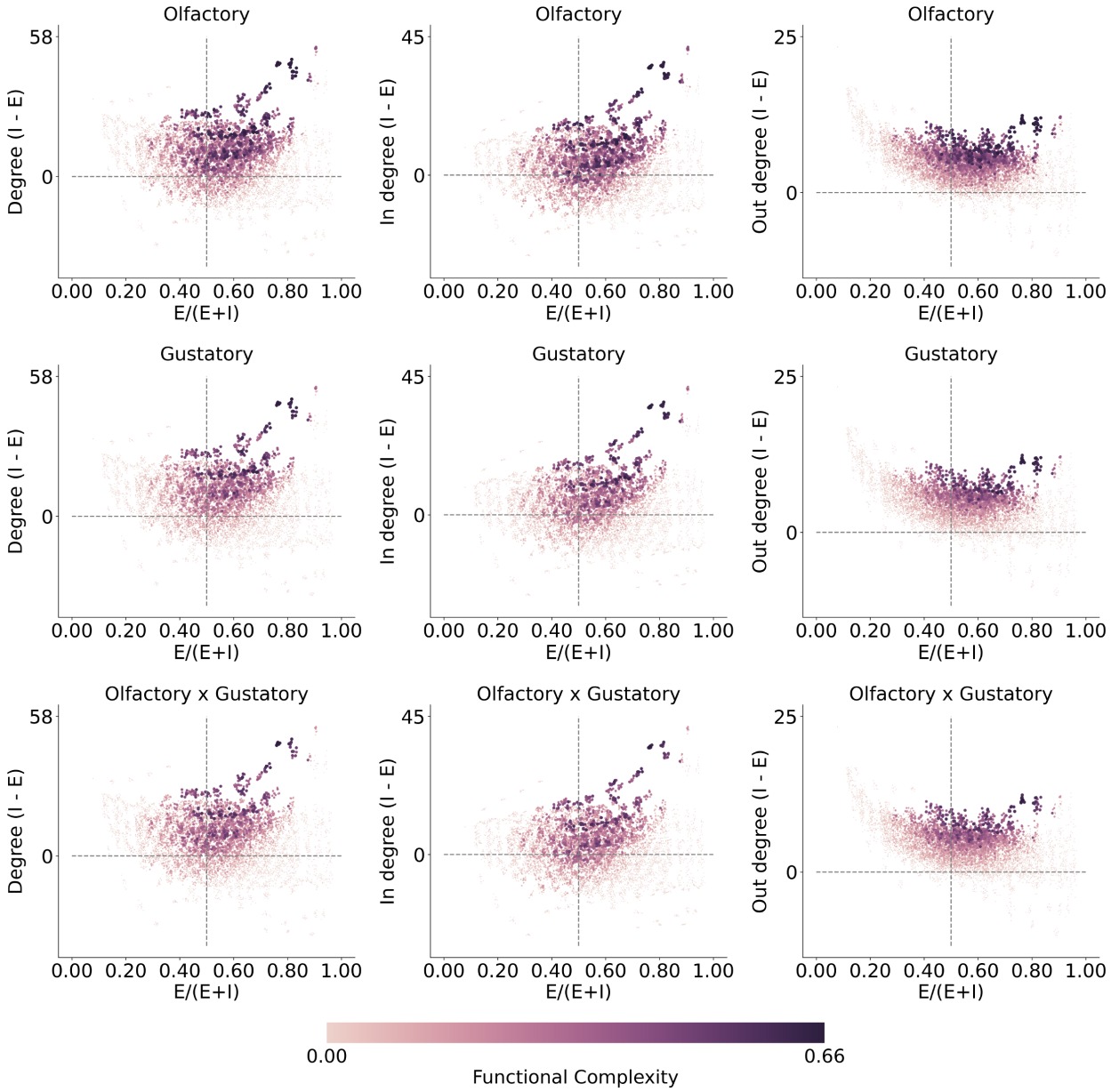

Figure A.9: **Related to Figure 3, functional complexity plotted separately across sensory modalities.** Degree-dependent sampling is based on in degree . Across sensory modalities (top to bottom) and degree quantification methods (left to right), networks of higher functional complexity (lighter color) have inhibitory neurons more highly connected than excitatory neurons (above horizontal gray line) and there is an over-abundance of excitatory neurons (right to vertical gray line).

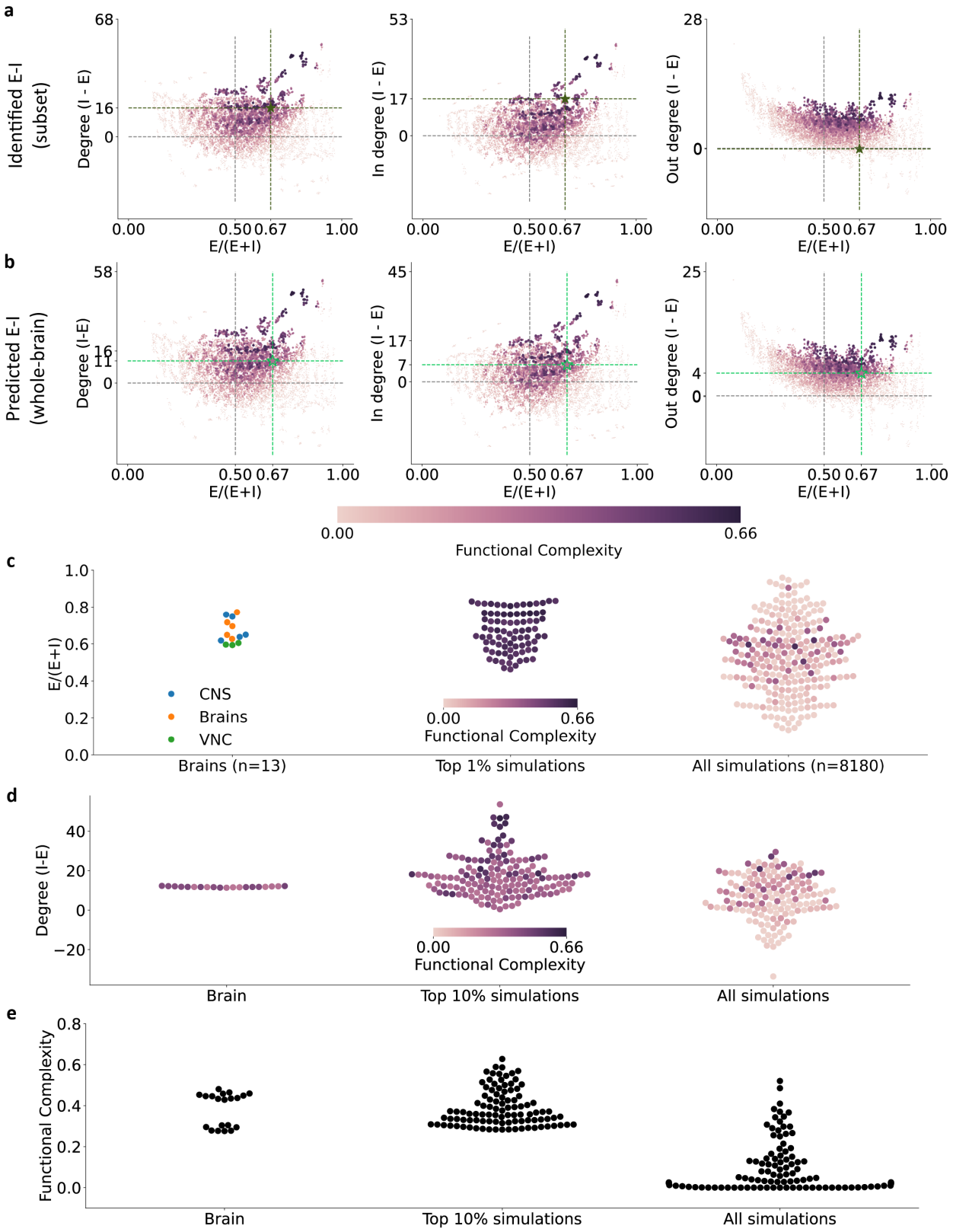

Figure A.10: **Same as Figure 3 except the degree-dependent sampling is based on in degree.** The mean E-I ratio of the top 13 group-averages and top 1% simulations are **not** statistical significantly different from the 13 brain E-I ratios (two-sided two-sample t-test, p-val: 0.97, 0.99 respectively); while the mean of all simulations are statistical significantly different from the brain observations (p-val: 0.03). Multiple comparisons corrected by Dunnett's.

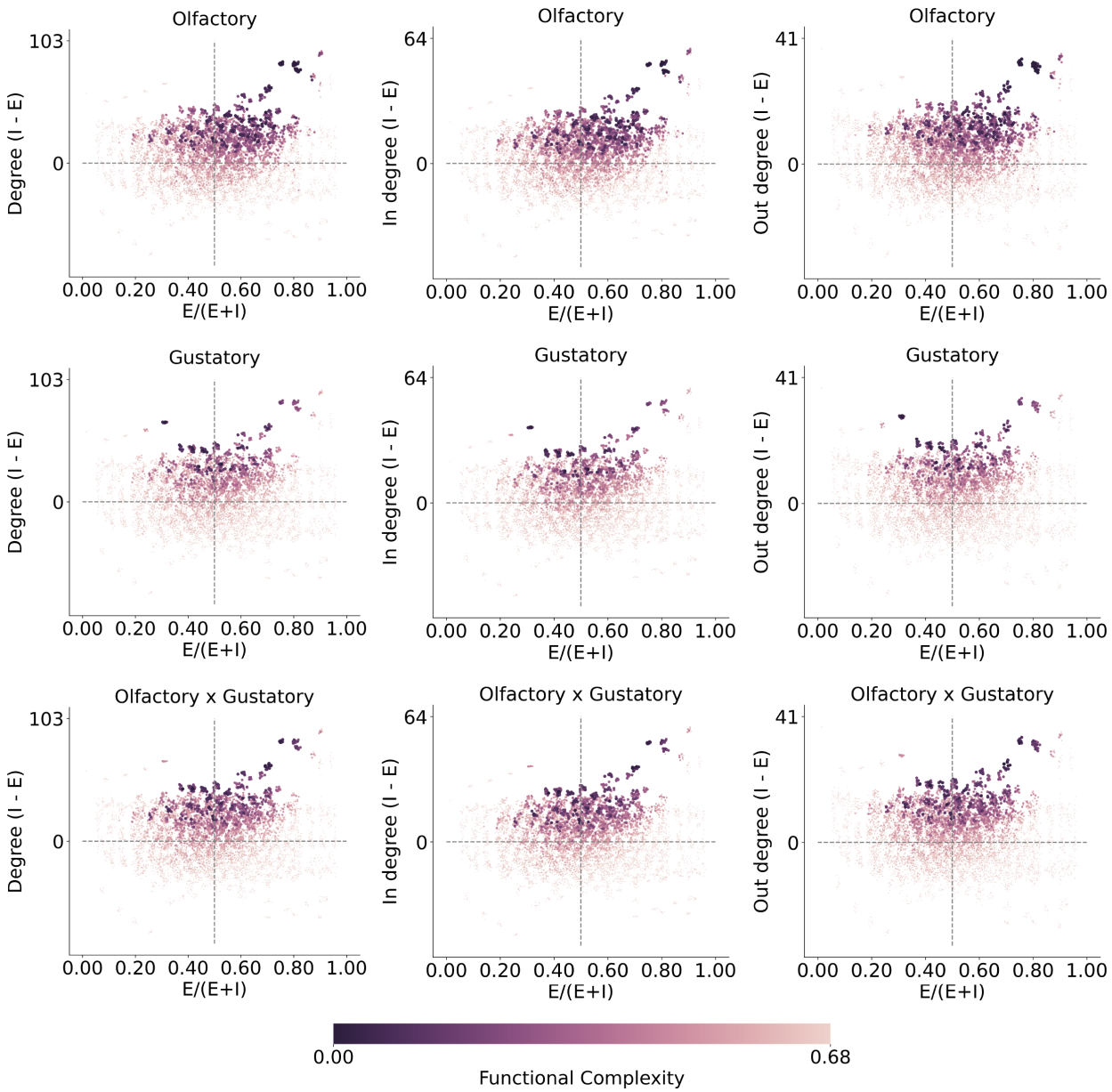

Figure A.11: **Related to Figure 3, functional complexity plotted separately across sensory modalities.** Degree-dependent sampling is based on in degree and the connection weight is given by all-all synaptic counts. Across sensory modalities (top to bottom) and degree quantification methods (left to right), networks of higher functional complexity (lighter color) have inhibitory neurons more highly connected than excitatory neurons (above horizontal gray line) and there is an over-abundance of excitatory neurons (right to vertical gray line).

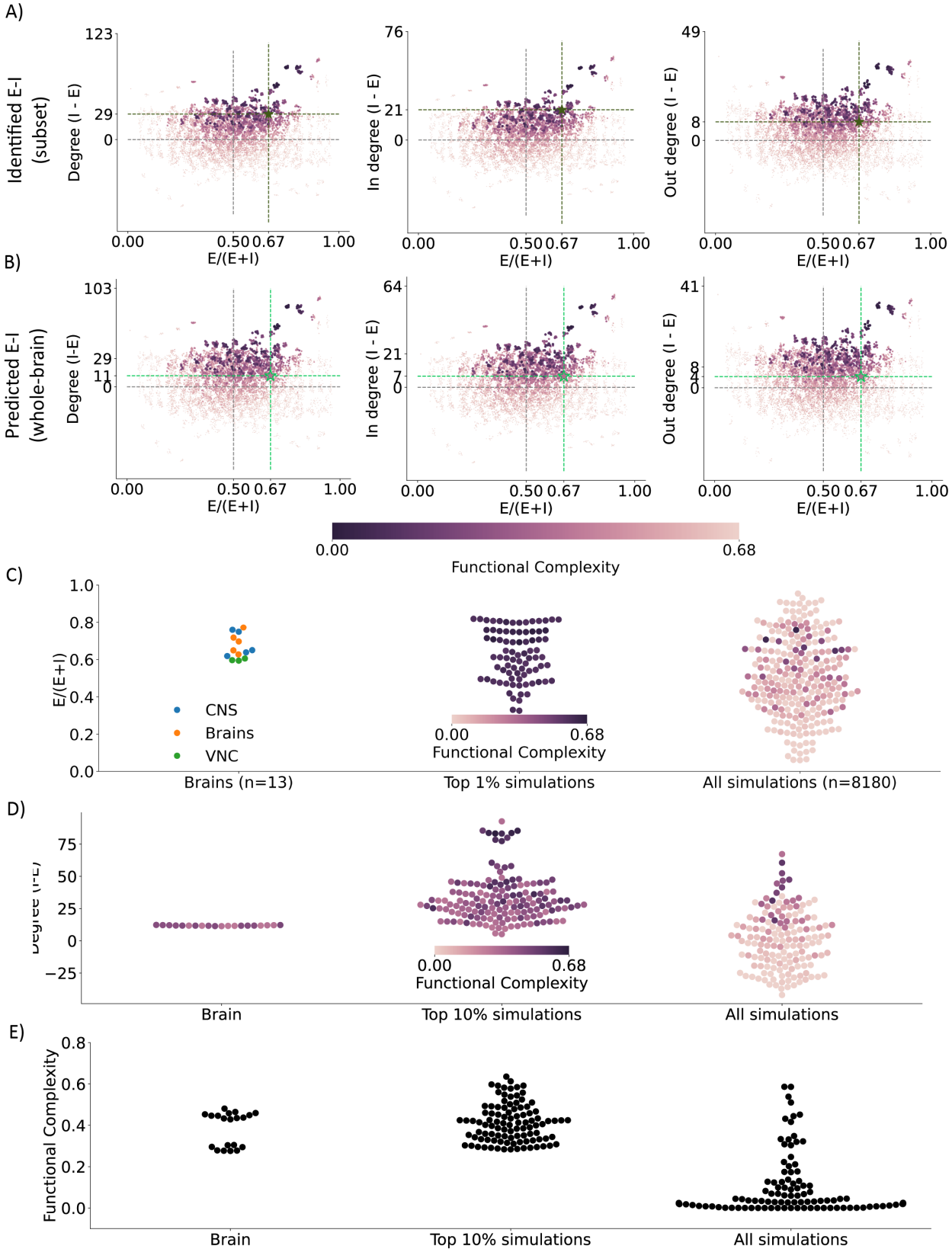

Figure A.12: **Same as Figure 3 except the degree-dependent sampling is based on in degree and including all-to-all synaptic counts as the EM constraint.** The mean E-I ratio of the top 13 group-averages and top 1% simulations are **not** statistical significantly different from the 13 brain E-I ratios (two-sided two-sample t-test, p-val: 0.65, 0.70 respectively); while the mean of all simulations are statistical significantly different from the brain observations (p-val: 0.01). Multiple comparisons corrected by Dunnett's.

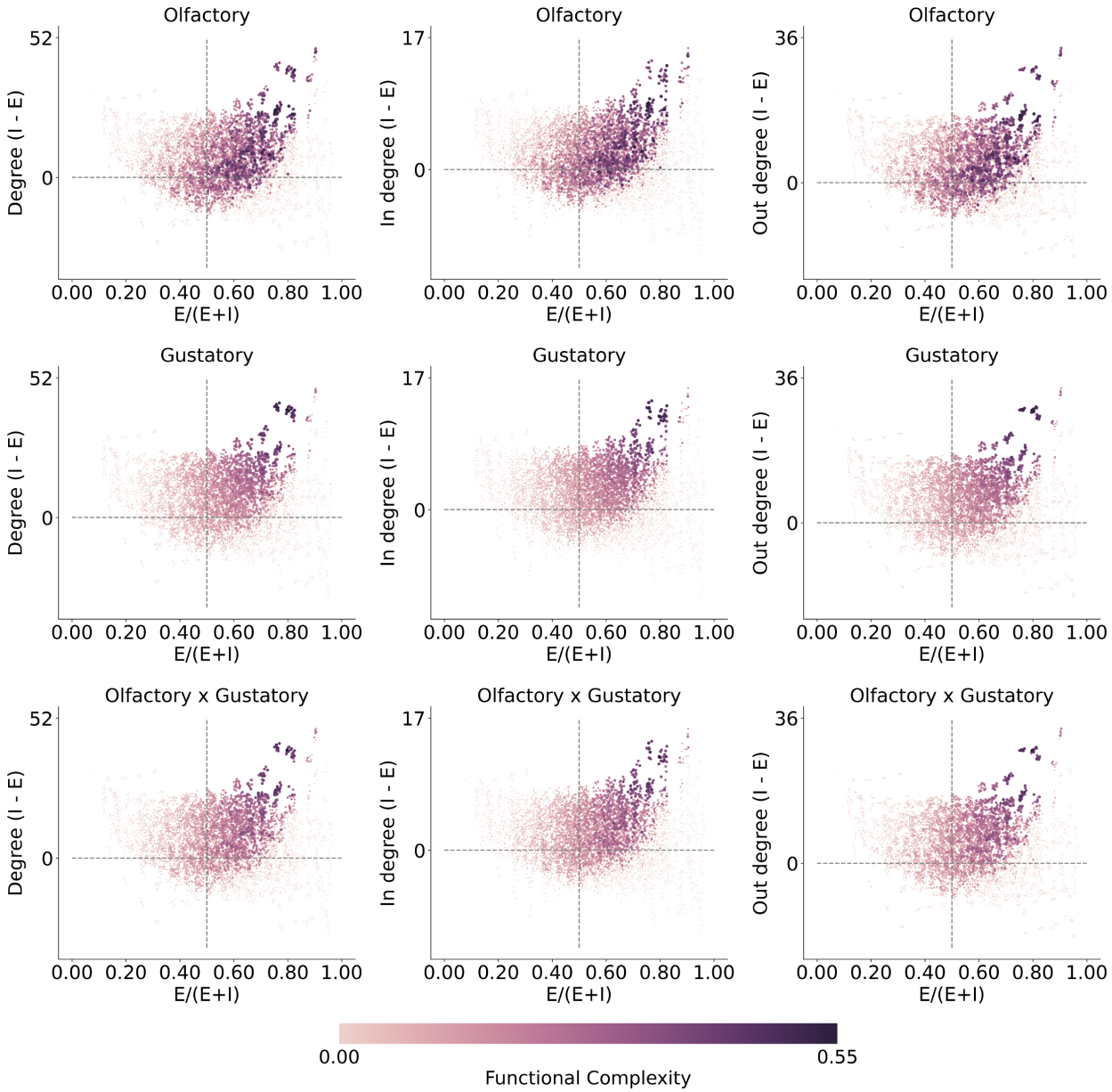

Figure A.13: **Related to Figure 3, functional complexity plotted separately across sensory modalities.** Degree-dependent sampling is based on out degree. Across sensory modalities (top to bottom) and degree quantification methods (left to right), networks of higher functional complexity (lighter color) have inhibitory neurons more highly connected than excitatory neurons (above horizontal gray line) and there is an over-abundance of excitatory neurons (right to vertical gray line).

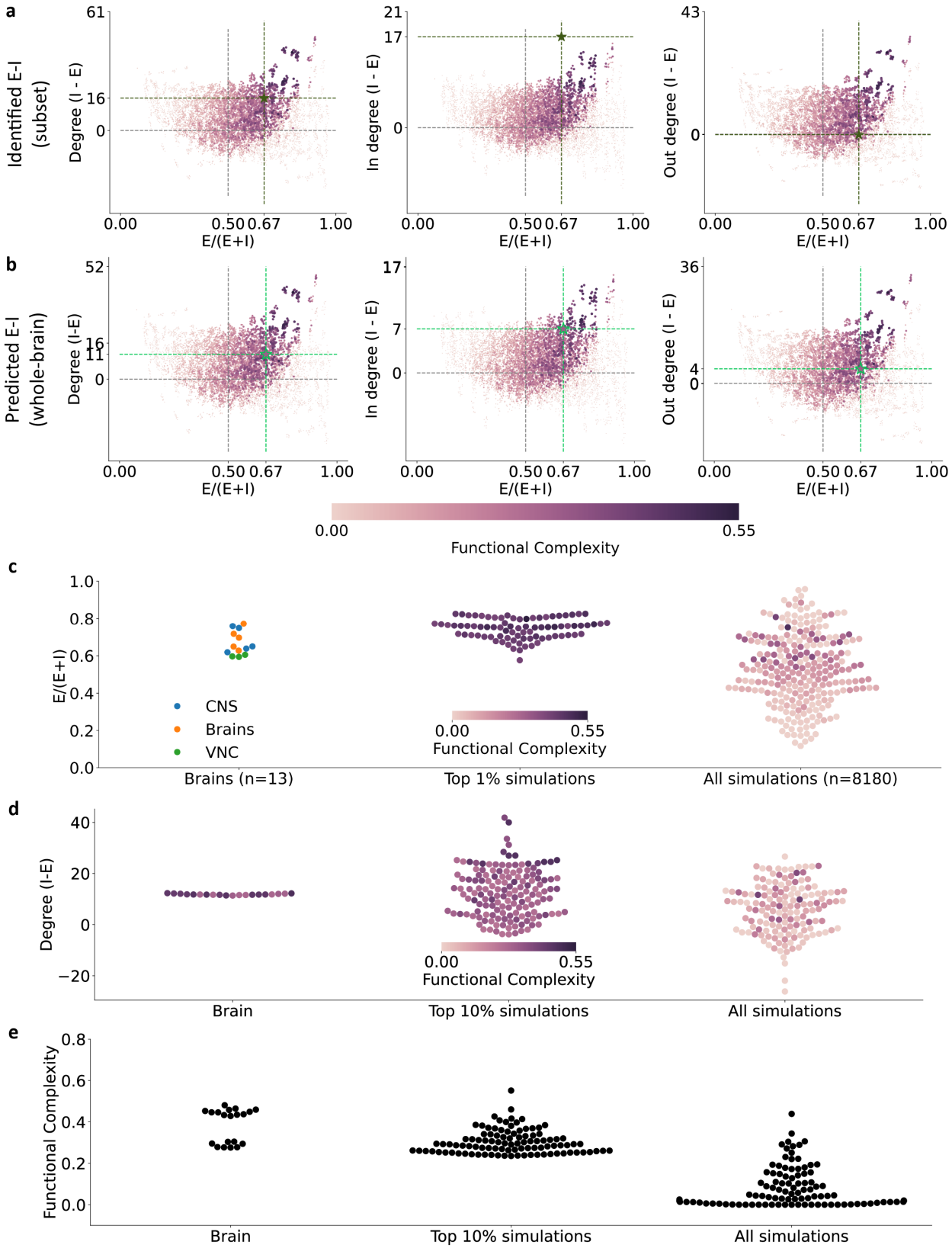

Figure A.14: **Same as Figure 3 except the degree-dependent sampling is based on out degree and including all-to-all synaptic counts as the EM constraint.** The mean E-I ratio of the top 13 group-averages and top 1% simulations are **not** statistical significantly different from the 13 brain E-I ratios (two-sided two-sample t-test, p-val: 0.51, 0.30 respectively); while the mean of all simulations are statistical significantly different from the brain observations (p-val: 0.03). Multiple comparisons corrected by Dunnett's.

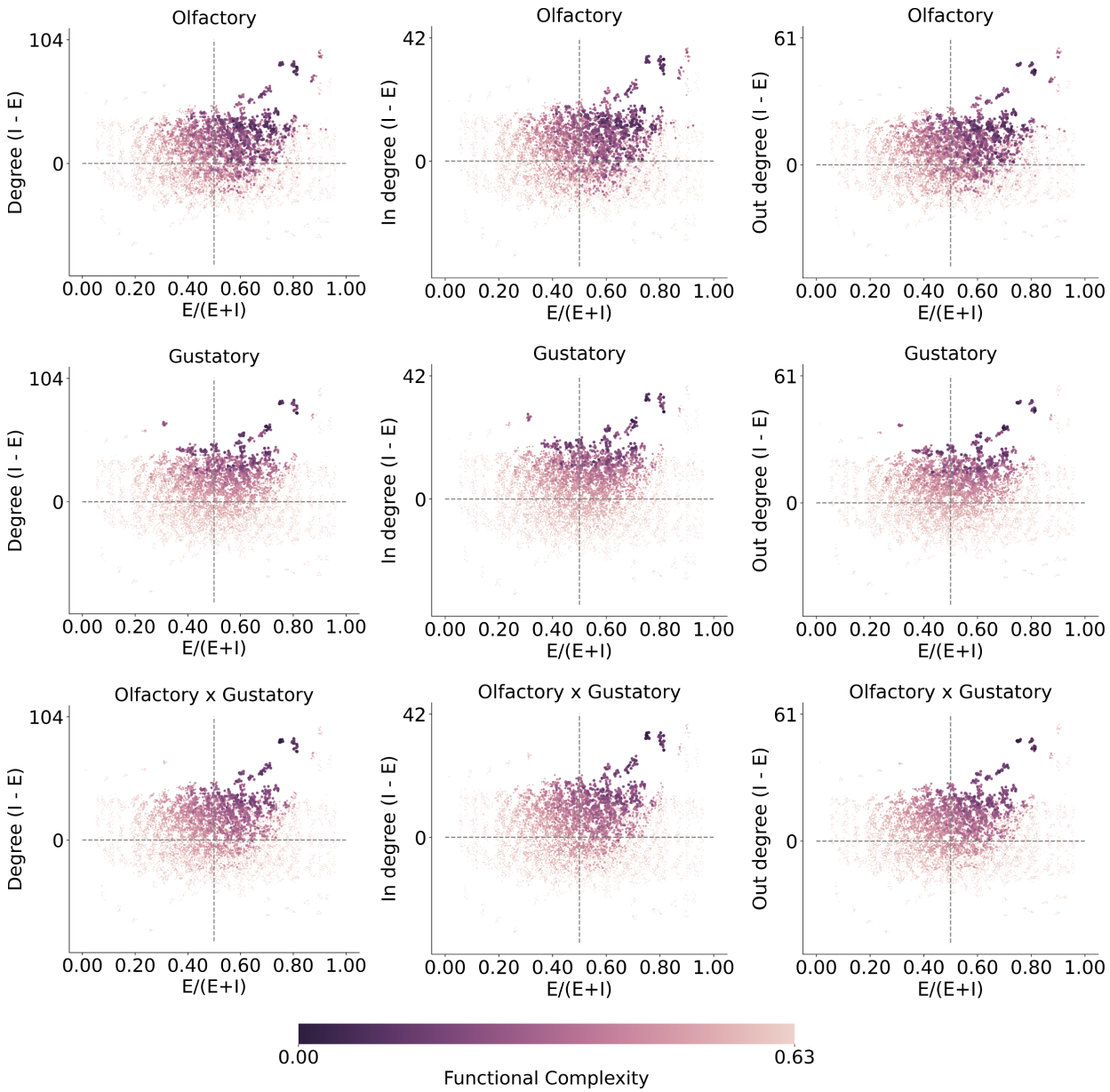

Figure A.15: **Related to Figure 3, functional complexity plotted separately across sensory modalities.** Degree-dependent sampling is based on out degree and the connection weight is given by all-all synaptic counts. Across sensory modalities (top to bottom) and degree quantification methods (left to right), networks of higher functional complexity (lighter color) have inhibitory neurons more highly connected than excitatory neurons (above horizontal gray line) and there is an over-abundance of excitatory neurons (right to vertical gray line).

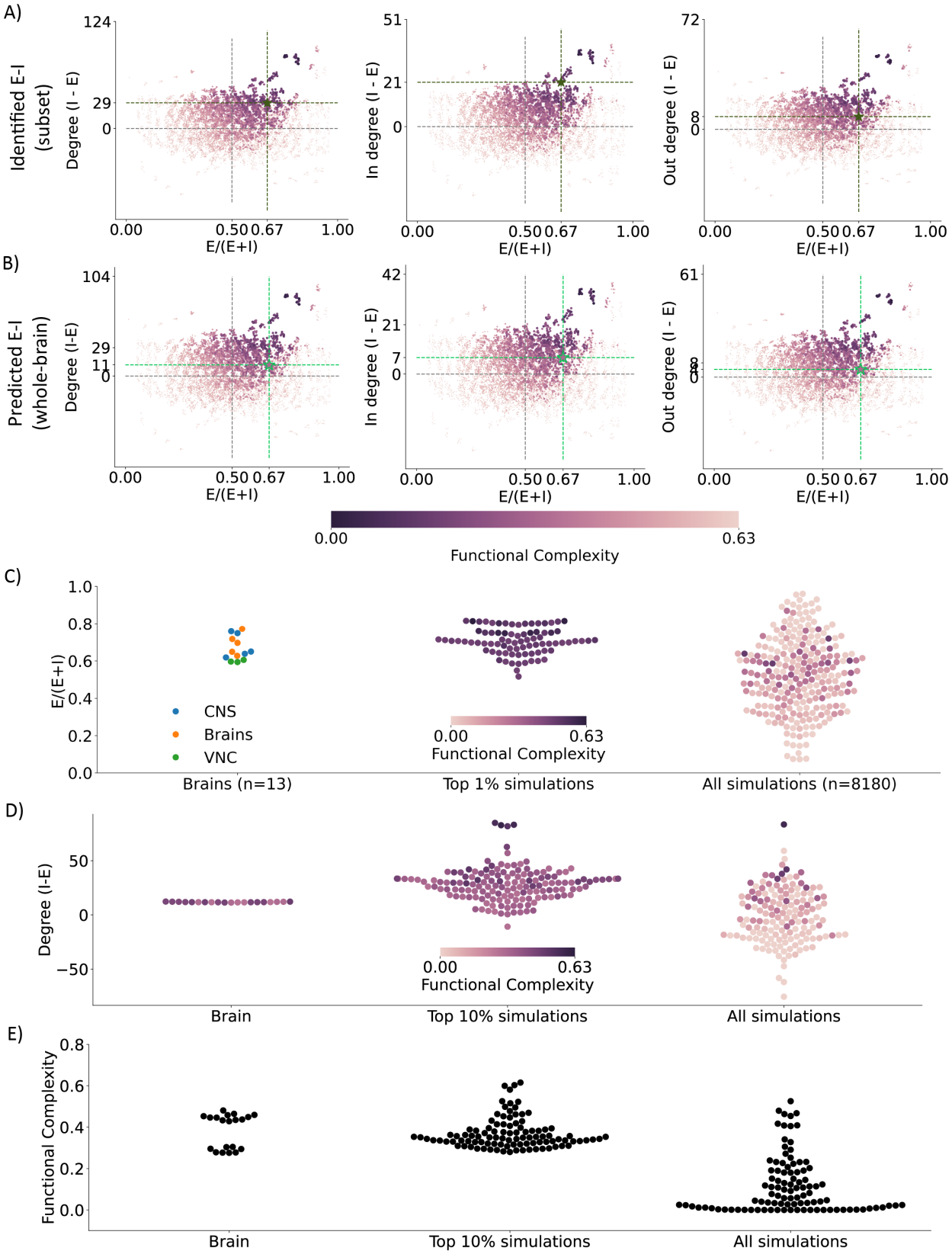

Figure A.16: **Same as Figure 3 except the degree-dependent sampling is based on out degree and including all-to-all synaptic counts as the EM constraint.** The mean E-I ratio of the top 13 group-averages and top 1% simulations are **not** statistical significantly different from the 13 brain E-I ratios (two-sided two-sample t-test, p-val: 0.92, 0.76 respectively); while the mean of all simulations are statistical significantly different from the brain observations (p-val: 0.01). Multiple comparisons corrected by Dunnett's.

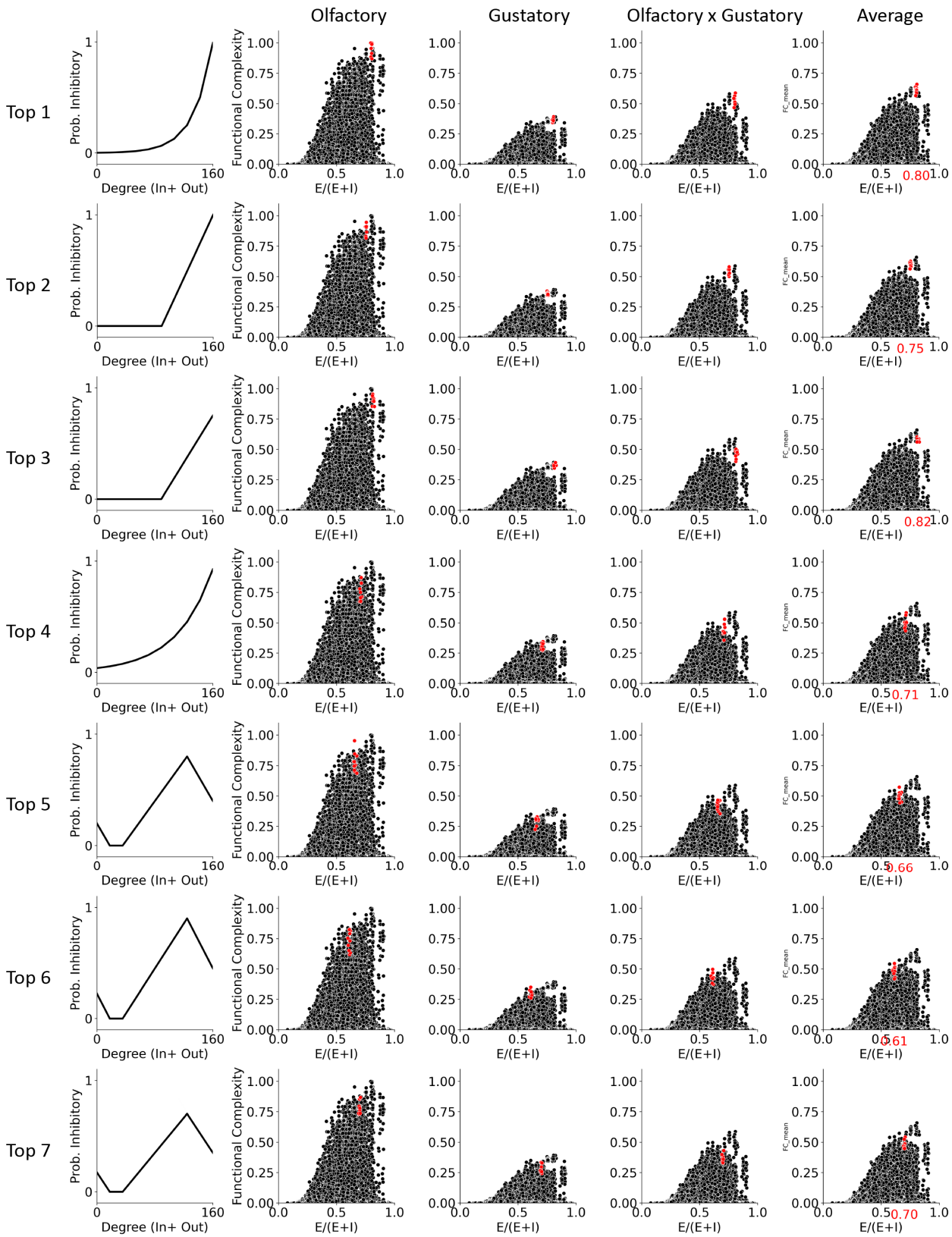

(cont'd on next page.)

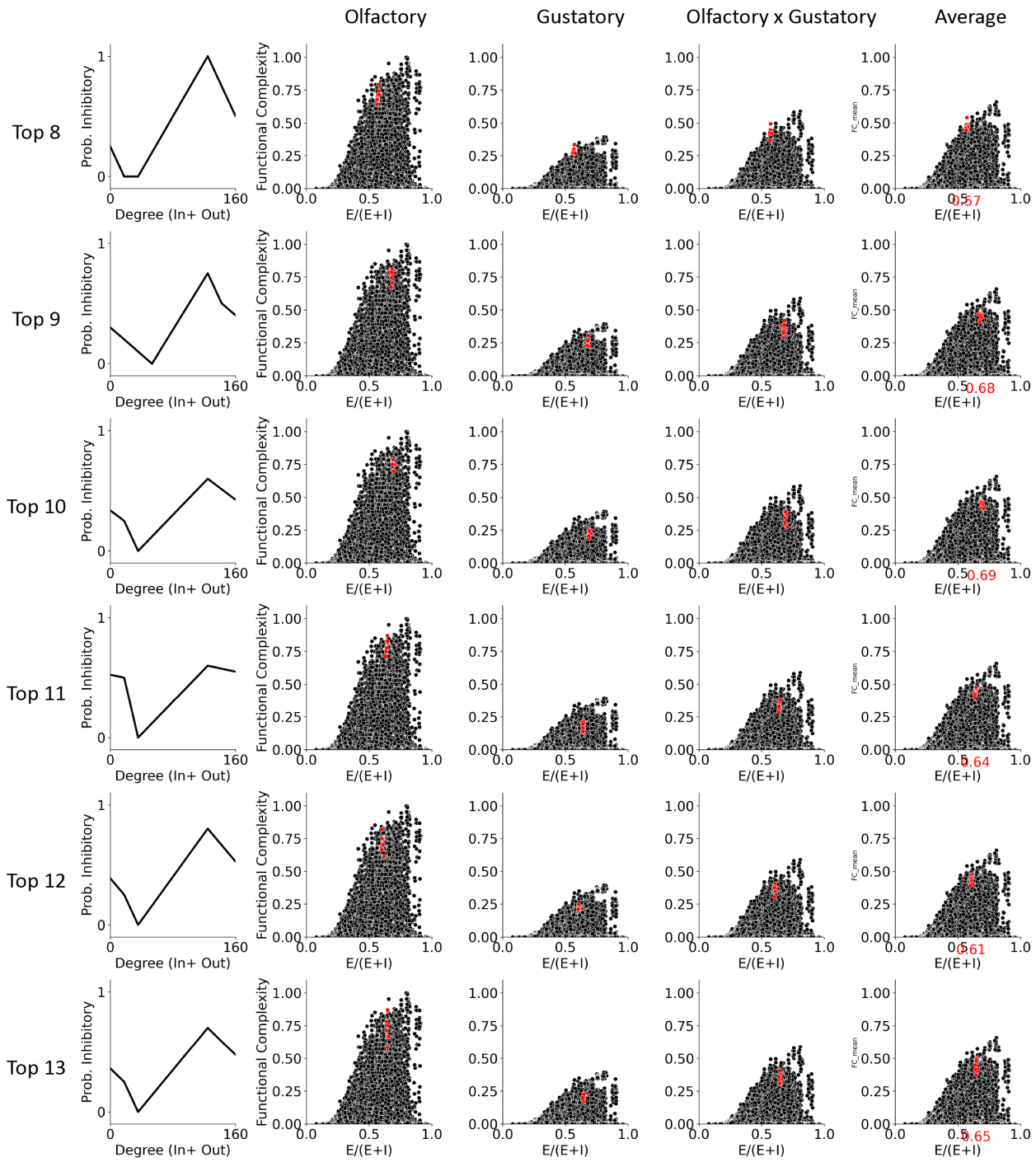

Figure A.17: **Top 13 degree-dependent E-I probability functions. (Related to Figure 3)** The top 13 E-I ratios plotted in Figure 3 middle left are delineated here. Top to bottom: the E-I probability function group that resulted in the highest functional complexity to lower.

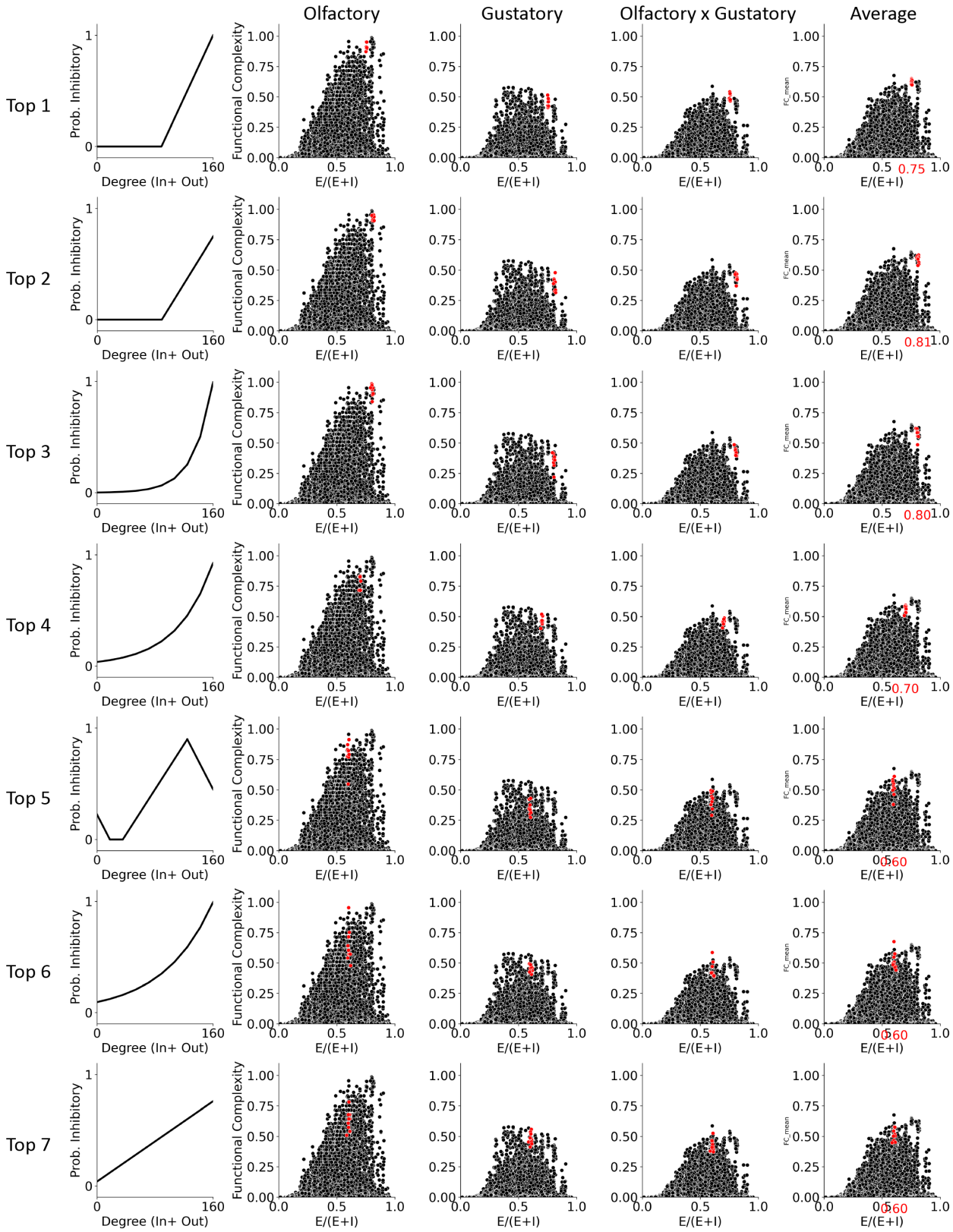

(cont'd on next page.)

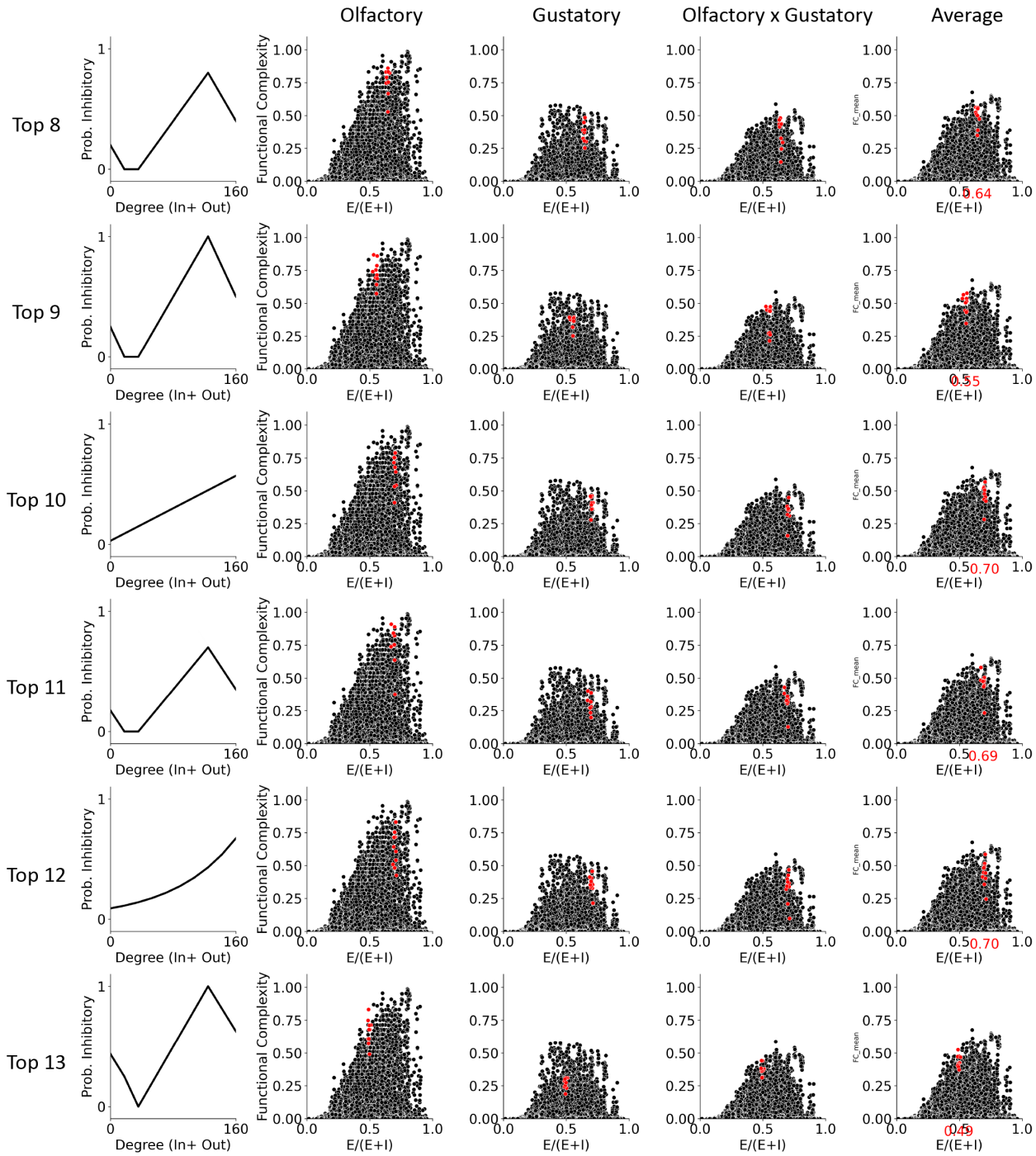

Figure A.18: **Same as Supplementary Figure A.17 except including all-to-all synaptic counts as the EM constraint.**

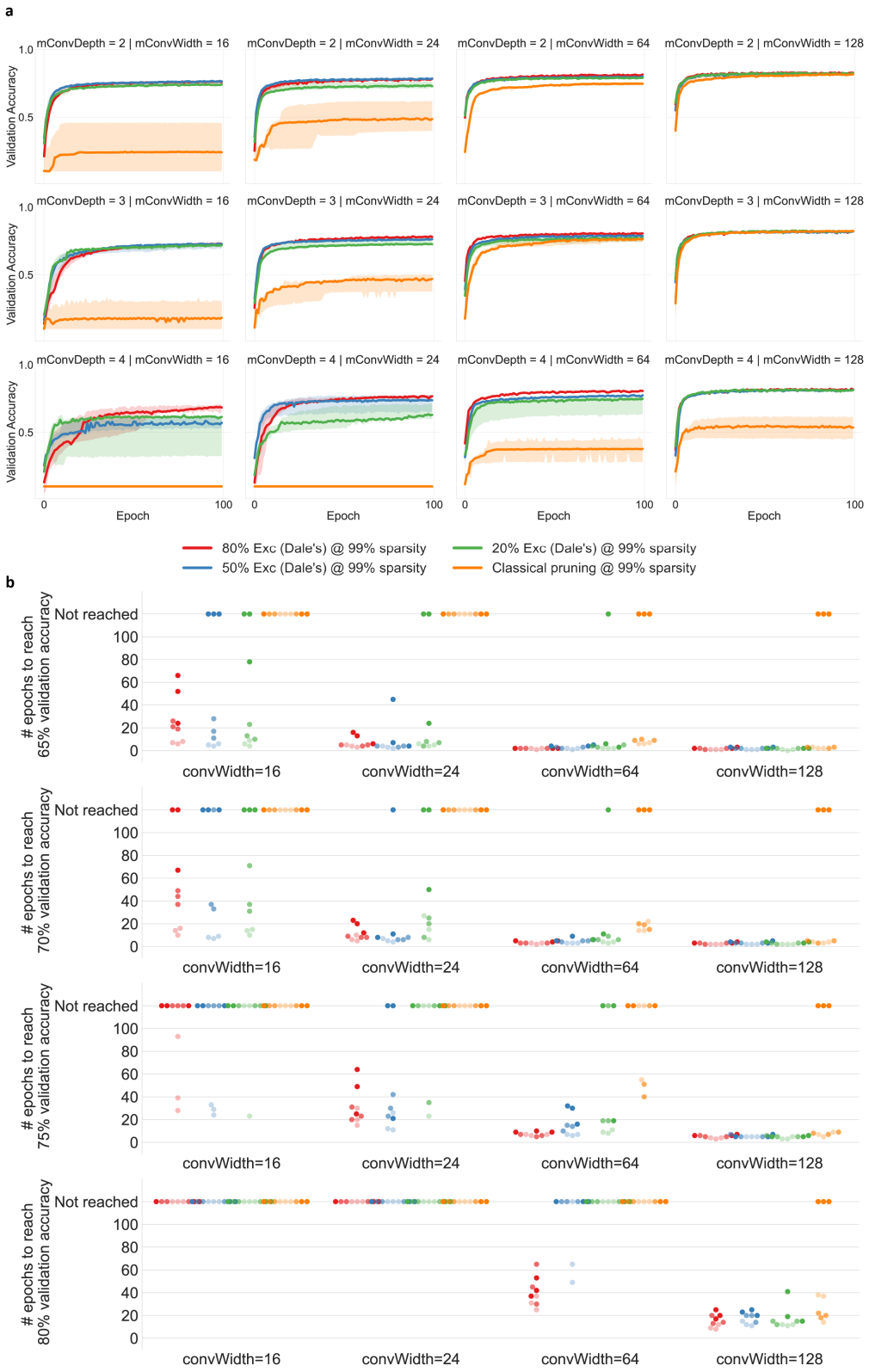

Figure A.19: **Related to Figure 5** A) Convolutional neural networks (CNNs) with 99% sparsity are trained with unconstained E-I configurations (orange, classical pruning setting), biologically constrained E-I configurations that follow the Dale's rule with 80% of excitatory neurons (red), 50% excitatory neurons (blue), and 20% excitatory neurons. Under classical pruning procedures (orange), CNNs of various depth (across rows) and width (across columns) can face difficulty in training at 99% sparsity, especially when the networks have narrow widths. These difficulties can be remedied by biologically constrained E-I configurations (blue, red, green). All plots are median with shaded area showing min and max (n=3). B) Computation efficiency results across more validation accuracy cut-offs.